Valence Trapping in Mixed-Valence $Mn^{II}Mn^{III}$ Complexes of a Macrocyclic Binucleating Ligand

Hsiu-Rong Chang,[1a] Scott K. Larsen,[2] Peter D. W. Boyd,[1b] Cortlandt G. Pierpont,*[,2] and David N. Hendrickson*[,1a]

Contribution from the School of Chemical Sciences, University of Illinois, Urbana, Illinois 61801, and the Department of Chemistry, University of Colorado, Boulder, Colorado 80309. *Received November 19, 1987*

Abstract: The electronic structures of two mixed-valence $Mn^{II}Mn^{III}$ complexes, $[LMn_2Cl_2Br]\cdot H_2O$ (**2**) and $[LMn_2Br_3]\cdot {}^1/_2CH_2Cl_2$ (**3**), and the Mn^{II}_2 complex LMn_2Cl_2 (**4**) are probed. The L^{2-} ligand is the dianion of the Schiff base condensation of 2 mol of 1,3-diaminopropane and 2 mol of 2,6-diformyl-4-*tert*-butylphenol. The X-ray structure of complex **4** has been determined by using direct methods to give discrepancy factors of $R = 0.0501$ and $R_w = 0.0697$ for 1884 observed ($|F| > 6.0\sigma|F|$) reflections. Complex **4** crystallizes in the triclinic space group $P\bar{1}$ with one molecule in a unit cell with dimensions $a = 7.270$ (1) Å, $b = 9.457$ (2) Å, $c = 12.316$ (2) Å, $\alpha = 108.36$ (1)°, $\beta = 94.92$ (1)°, and $\gamma = 99.58$ (1)°. The observed and calculated densities are 1.39 (2) and 1.41 g cm^{-3}, respectively. The L^{2-} ligand in LMn_2Cl_2 is essentially planar, with the Mn^{II} ions displaced by 0.69 Å on either side of the ligand plane. The Mn···Mn distance is 3.168 (3) Å. The X-ray structure of complex **2** has been determined by using direct methods to give $R = 0.0711$ and $R_w = 0.0974$ for 1732 observed ($|F| > 6.0\sigma|F|$) reflections. Complex **2** crystallizes in the monoclinic space group $C2/c$ with 8 molecules in a unit cell with dimensions $a = 21.064$ (7) Å, $b = 13.559$ (4) Å, $c = 27.652$ (6) Å, and $\beta = 105.51$ (2)°. The observed and calculated densities are 1.38 (2) and 1.34 g cm^{-3}. The structural results for $[LMn_2Cl_2Br]\cdot H_2O$ show that this complex is valence trapped. The Mn^{III} ion has an average Mn–O length of 1.936 (10) Å, while the Mn^{II} ion exhibits Mn–O lengths of 2.129 (10) and 2.386 (11) Å. The Mn^{III} ion is coordinated axially to two halide ions and is 0.15 Å out of the ligand–atom plane. The Mn^{II} ion is displaced 1.25 Å from the ligand–atom plane on the opposite side and interacts with one of the halide ions coordinated to the Mn^{III} ion. Electrochemical results are presented for LMn_2X_2 (X = Cl or Br) to show that these complexes have two one-electron oxidation waves at ca. +0.6 and ca. +1.2 V vs NHE. Variable-temperature magnetic susceptibility data are fit to give magnetic exchange parameters of +0.24, −2, and −1 cm^{-1} for complexes **4**, **2**, and **3**, respectively. Similar EPR data are found for the two mixed-valence complexes. At 7.5 K a glass of **3** gives an X-band spectrum with a broad $g = 2$ signal and apparent fine structure signals at $g = 29.0$, 7.4, 5.4, and 4.1. A combination of Orbach relaxation processes involving low-lying spin states and modulation of the g_x, g_y values for the ground doublet by strain effects on the magnitude of the isotropic exchange and/or single-ion zero-field splitting are suggested as the origin of the absence of resolution of manganese hyperfine structure in the $g = 2$ signal. Relatively weak antiferromagnetic interactions are seen for the five known binuclear $Mn^{II}Mn^{III}$ complexes, whereas, strong antiferromagnetic interactions are found for the five known binuclear $Mn^{III}Mn^{IV}$ complexes. The possible causes of this difference in magnitude of exchange interactions are discussed.

There are two different multinuclear manganese enzymes known. Two manganese ions per protein subunit are believed[3] to be present in the pseudocatalase from *Lactobacillus planatrum*, an enzyme which catalyzes the disproportionation of H_2O_2. Two to four manganese ions,[4] perhaps in conjunction with a redox-active component of the protein,[4b,c] serve as the active site for catalyzing the oxidation of two molecules of H_2O to give one molecule of O_2 in photosynthesis. The Mn_x aggregate in photosystem II (PSII) cycles between five distinct oxidation levels labeled S_0, S_1, S_2, S_3, and S_4 in the pioneering work of Joliot et al.[5] and Kok et al.[6] The S_n states contain manganese ions in various combinations of oxidation states, including Mn^{II}, Mn^{III}, and Mn^{IV}, and ligation is provided by O and N atoms from amino acid residues.[7]

A limited number of model multinuclear manganese complexes has been well characterized. Included are a few binuclear Mn^{II}_2 complexes bridged by alkoxide,[8] hydroxide,[8] and chloride[8] ions, as well as H-bonding interactions,[9] and those with no bridges.[10] Only two binuclear Mn^{III}_2 complexes, each with one μ-oxo and two μ-acetato bridges, have been well documented.[11,12]

Recently two research groups[13,14] independently reported an EPR signal for the S_2 state of PSII. This signal has been attributed to either a binuclear $Mn^{III}Mn^{IV}$ site[13] or a tetranuclear $Mn^{III}_3Mn^{IV}$ site.[15] Even though the origin and exact characteristics of this S_2 EPR signal with 16–18 manganese hyperfine lines are matters of active discussion, vis-a-vis detailed power

(1) (a) University of Illinois. (b) On leave at the University of Illinois from the University of Auckland, Auckland, New Zealand.
(2) University of Colorado.
(3) (a) Kono, Y.; Fridovich, I. *J. Biol. Chem.* **1983**, *258*, 6015. (b) Beyer, W. F., Jr.; Fridovich, I. *Biochemistry* **1985**, *24*, 6460.
(4) (a) Dismukes, G. C. *Photochem. Photobiol.* **1986**, *43*, 99–115. (b) Govindjee; Kambara, T.; Coleman, W. *Photochem. Photobiol.* **1985**, *42*, 187–210. (c) Kambara, T.; Govindjee *Proc. Natl. Acad. Sci. U.S.A.* **1985**, *82*, 6119–6123. (d) Webber, A. N.; Spencer, L.; Sawyer, D. T.; Heath, R. L. *FEBS Lett.* **1985**, *189*, 258–262. (e) Amesz, J. *Biochim. Biophys.* **1983**, *726*, 1–12. (f) Livorness, J.; Smith, T. D. *Struct. Bonding (Berlin)* **1982**, *48*, 2–44. (g) Sauer, K. *Acc. Chem. Res.* **1980**, *13*, 249–256. (h) Radmer, R.; Cheniae, G. In *Topics in Photosynthesis*; Barber, J., Ed.; Elsevier: Amsterdam, 1977. (i) Dismukes, G. C. *The Organization and Function of Manganese in the Water-Oxidizing Complex of Photosynthesis*; Academic: New York, 1986; Chapter 16; p 275. (j) Renger, G. *Angew. Chem., Int. Ed. Engl.* **1987**, *26*, 643–660.
(5) Joliot, P.; Barbieri, G.; Chabaud, R. *Photochem. Photobiol.* **1969**, *10*, 302.
(6) Kok, B.; Forbush, B.; McGloin, M. P. *Photochem. Photobiol.* **1970**, *11*, 457.
(7) (a) See ref 4a and 4e. (b) Takohashi, Y.; Katoh, S. *Biochim. Biophys. Acta* **1986**, *848*, 183. (c) Yachandra, V. K.; Guiles, R. D.; McDermott, A.; Britt, R. D.; Dexheimer, S. L.; Sauer, K.; Klein, M. P. *Biochim. Biophys. Acta* **1986**, *850*, 324. (d) Guiles, R. D.; Yachandra, V. K.; McErmott, A. E.; Britt, K. D.; Dexheimer, S. L.; Sauer, K.; Klein, M. P. In *Proc. VII Int. Congr. Photosynth.*, in press.
(8) Mathur, P.; Crowder, M.; Dismukes, G. C. *J. Am. Chem. Soc.* **1987**, *109*, 5227–5233.
(9) Laskowski, E. J.; Hendrickson, D. N. *Inorg. Chem.* **1978**, *17*, 457.
(10) Okawa, H.; Honda, A.; Nakamura, M.; Kida, S. *J. Chem. Soc., Dalton Trans.* **1985**, 59–64.
(11) Wieghardt, K.; Bossek, V.; Ventur, D.; Weiss, J. *J. Chem. Soc., Chem. Commun.* **1985**, 347.
(12) Sheats, J. E.; Czernuszewicz, R. S.; Dismukes, G. C.; Rheingold, A. L.; Petrouleas, V.; Stubbe, J.; Armstrong, W. H.; Beer, R. H.; Lippard, S. J. *J. Am. Chem. Soc.* **1987**, *109*, 1435–1444.
(13) Dismukes, G. C.; Siderer, Y. *Proc. Natl. Acad. Sci. U.S.A.* **1981**, *78*, 274–278.
(14) Hansson, Ö.; Andreasson, L. E. *Biochim. Biophys. Acta* **1982**, *679*, 261–268.
(15) Dismukes, G. C.; Ferris, K.; Watnick, P. *Photobiochem. Photobiophys.* **1982**, *3*, 243–256.

0002-7863/88/1510-4565$01.50/0 © 1988 American Chemical Society

Table I. Microanalytical Data for Binuclear Manganese Complexes

compound		% C	% H	% N	% Mn	% Cl	% Br
$[LMn_2Cl_2]\cdot{}^1/_2CH_3OH$	obsd	53.70	5.93	8.15	16.07	10.78	
	calcd	53.58	5.86	8.20	16.08	10.37	
$[LMn_2Br_2]\cdot{}^1/_2CH_3OH$	obsd	47.57	5.26	7.27	14.64		20.76
	calcd	47.42	5.22	7.25	14.22		20.71
$[LMn_2Cl_2Br]\cdot 2H_2O$	obsd	45.95	5.18	7.04	14.23	9.33	10.51
	calcd	45.99	5.40	7.15	14.02	9.05	10.21
$[LMn_2Br_3]\cdot{}^1/_2CH_2Cl_2$	obsd	41.35	4.62	6.40	12.37	4.36	27.17
	calcd	41.69	4.47	6.38	12.50	4.03	27.28
$[LMn_2Cl_2]$	obsd	53.77	5.75	8.44	16.26	10.96	
	calcd	53.93	5.69	8.39	16.46	10.92	

saturation, temperature dependence, and sample history studies,[16] the observation of this EPR signal has spawned a growing interest in characterizing mixed-valence multinuclear manganese complexes. Until very recently only salts of the $Mn^{III}Mn^{IV}$ complex

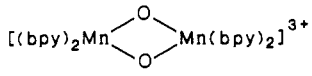

and the analogous bipyridine (bpy) *N*-oxide and phenanthroline (phen) complexes have been characterized.[17] In the last year Wieghardt et al.[18] and Bashkin et al.[19] each reported one new binuclear $Mn^{III}Mn^{IV}$ complex, both of which exhibit interesting $g = 2$ EPR signals with considerable manganese hyperfine structure resembling that of the S_2 EPR signal.

Very recently reports of binuclear $Mn^{II}Mn^{III}$ complexes have appeared. Mabad et al.[20] noted that a $Mn^{II}Mn^{III}$ complex generated by O_2 oxidation of a Mn^{II}_2 Schiff-base complex also gave a 16-line EPR signal. The X-ray structure of this complex could not be reported due to the difficulty of growing suitable crystals. The X-ray structures of the $Mn^{II}Mn^{III}$ complexes $[Mn_2(bpmp)(\mu\text{-}OAc)_2](ClO_4)_2\cdot H_2O$ (**1**) and $[LMn_2Cl_2Br]\cdot H_2O$ (**2**) were just communicated.[21] The ligands $bpmp^-$ and L^{2-} are

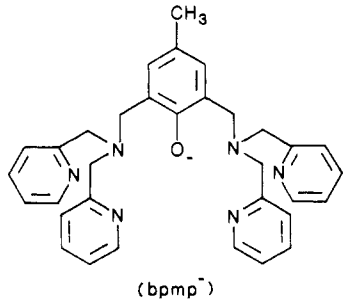

$(bpmp^-)$

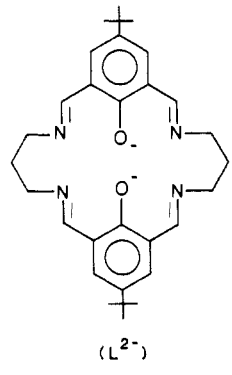

(L^{2-})

In this paper detailed magnetochemistry, EPR, and electrochemistry data are presented for **2**, mixed-valence $[LMn_2Br_3]\cdot{}^1/_2CH_2Cl_2$ (**3**), and the Mn^{II}_2 complex LMn_2Cl_2 (**4**), together with the X-ray structures of **2** and **4**.

Experimental Section

Compound Preparation. Most reactants and solvents used in preparing **2**, **3**, and **4** are commercially available and were used without further purification. 2,6-Diformyl-4-*tert*-butylphenol was synthesized by using a procedure similar to that described by Desmond.[22] An outline of the synthesis is shown below:

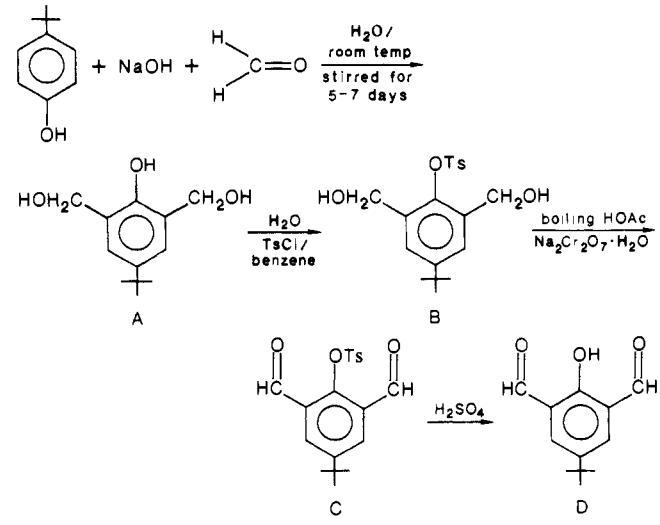

NaOH (130 g, 3.25 mol) was dissolved in 2.4 L of H_2O and then 300 g (2.0 mol) of 4-*tert*-butylphenol were added. The mixture was heated slightly in order to dissolve the solids. After the solution was cooled to room temperature, 350 mL (4.3 mol) of 37% formaldehyde were added. The orange solution was stirred at room temperature for 5–7 days; 220 mL of concentrated HCl were added to this solution and the H_2O phase was decanted off. The organic phase was washed three times with 700-mL portions of distilled H_2O. Some 1400 mL of $CHCl_3$ were added to the organic phase and dried for ~4 h over 200 g of anhydrous $MgSO_4$. The solution was filtered with a fine frit and then cooled in a dry ice/acetone bath. While the solution was cooling, the wall of the container was scratched to induce precipitation of A. This precipitate was washed with 15 mL of $CHCl_3$ and dried to yield 310 g (1.48 mol) of 4-*tert*-butyl-2,6-bis(hydroxymethyl)phenol (A). Then all of A was deprotonated by dissolving all 310 g of A in a solution containing 75 g (1.9 mol) of NaOH in 490 mL of H_2O. To the resulting solution were added 294 g (1.54 mol) of tosyl chloride (TsCl) in 326 mL of benzene. The mixture was stirred for 2 days and then the tosylated compound B was collected by filtration, followed by washing with benzene three times. Next 189 g (0.52 mol) of compound B were dissolved in 745 mL of glacial acetic acid. The solution was heated and stirred until boiling. While the solution was boiling, 161 g (0.50 mol) of $Na_2Cr_2O_7\cdot H_2O$ were *very slowly* added; then, the solution was cooled and the green acidic solution was decanted off. The precipitate was washed with water, pulverized into small particles, and then washed with 1:1 ethanol/H_2O solution. Then this compound C must be recrystallized from hot 2:1 ethanol/H_2O solution (~600 mL of the ethanol/H_2O solution was used). This recrystallization procedure is very important, for if compound C is not pale green or white, the recrystallization procedure should be repeated since the yield of 4-*tert*-butyl-2,6-diformylphenol in the final reaction is very dependent on the purity of compound C. Finally, 110 g (0.30 mol) of

(16) (a) dePaula, J. C.; Brudvig, G. W. *J. Am. Chem. Soc.* **1985**, *107*, 2643–2648. (b) DePaula, J. C.; Beck, W. F.; Brudvig, G. W. *J. Am. Chem. Soc.* **1986**, *108*, 4002–4009. (c) Hansson, Ö.; Aasa, R.; Vänngård, T. *Biophys. J.* **1987**, *51*, 825–832. (d) Zimmermann, J.-L.; Rutherford, A. W. *Biochemistry* **1986**, *25*, 4609–4615. (e) dePaula, J. C.; Innes, J. B.; Brudvig, G. W. *Biochemistry* **1985**, *24*, 8114–8120.

(17) (a) Cooper, S. R.; Dismukes, G. C.; Klein, M. P.; Calvin, M. *J. Am. Chem. Soc.* **1978**, *100*, 7248. (b) Inoue, M. *Bull. Chem. Soc. Jpn.* **1978**, *51*, 1400. (c) Cooper, S. R.; Calvin, M. *J. Am. Chem. Soc.* **1977**, *99*, 6623. (d) Plaskin, P. M.; Stoufer, R. C.; Mathew, M.; Palenik, G. J. *J. Am. Chem. Soc.* **1972**, *94*, 2121. (e) Stebler, M.; Ludi, A.; Bürgi, H.-B. *Inorg. Chem.* **1986**, *25*, 4743–4750.

(18) Weighardt, K.; Bossek, U.; Zsolnai, L.; Huttner, G.; Blondin, G.; Girerd, J.-J.; Babonneau, F. *J. Chem. Soc., Chem. Commun.* **1987**, 651–653.

(19) Bashkin, J. S.; Schake, A. R.; Vincent, J. B.; Huffman, J. C.; Christou, G.; Chang, H.-R.; Li, Q.; Hendrickson, D. N., submitted for publication.

(20) Mabad, B.; Tuchagues, J.-P.; Hwang, Y. T.; Hendrickson, D. N. *J. Am. Chem. Soc.* **1985**, *107*, 2801–2802.

(21) Diril, H.; Chang, H.-R.; Larsen, S. K.; Potenza, J. A.; Pierpont, C. G.; Schugar, H. J.; Isied, S. S.; Hendrickson, D. N. *J. Am. Chem. Soc.* **1987**, *109*, 6207–6208.

(22) Desmond, M. Ph.D. Thesis, University of Illinois, 1979.

compound C were added to 135 mL of concentrated H_2SO_4 and the mixture was stirred for 30 min. This acidic solution was decanted into a 1500-mL water/ice mixture and then stirred for 2 h. The resulting brownish red solid was filtered and then washed with water. Some 3 L of hexane was used to extract the product. After the hexane was removed by evaporation, the yellow solid was recrystallized from diethyl ether. Some 16 g of brownish-yellow product D were obtained; mp 95 ± 1 °C. Anal. Calcd for $C_{12}H_{14}O_3$: C, 69.89; H, 6.84. Found: C, 69.75; H, 6.83.

Samples of the binuclear Mn^{II}_2 complex $[LMn_2Cl_2]\cdot{}^1/_2CH_3OH$ and $[LMn_2Br_2]\cdot{}^1/_2CH_3OH$ were prepared by employing a metal template reaction as first reported by Pilkington and Robson[23] in 1970. To a solution of 1.77 g (8.94 mmol) of $MnCl_2\cdot4H_2O$ [or 2.62 g (9.13 mmol) of $MnBr_2\cdot4H_2O$] and 2.20 g (8.98 mmol) of $Mn(OAc)_2\cdot4H_2O$ in 90 mL of methanol were added, in turn, 1.53 mL (17.9 mmol) of 1,3-diaminopropane in 10 mL of CH_3OH and 2.954 g (14.3 mmol) of 2,6-diformyl-4-*tert*-butylphenol in 90 mL of CH_3OH. The resulting solution was heated at the boiling point for 15 min during which time yellow crystals of $[LMn_2Cl_2]\cdot{}^1/_2CH_3OH$ (or $[LMn_2Br_2]\cdot{}^1/_2CH_3OH$) separated from the hot solution. The solid was collected and washed with hot methanol several times. Finally, the microcrystalline product was dried in the air for $^1/_2$ h by means of an oil bath at 100 °C. Analytical data for these two $[LMn_2X_2]\cdot{}^1/_2CH_3OH$ compounds are collected in Table I. The single crystal of LMn_2Cl_2 (**4**) used in the structure determination was grown in a diffusion method. $[LMn_2Cl_2]\cdot{}^1/_2CH_3OH$ was dissolved in CH_2Cl_2 and then CH_3CN was carefully layered on top of the CH_2Cl_2 solution. It took about 1 week of diffusing the CH_3CN into the CH_2Cl_2 to obtain a crystal of reasonable size. The analytical data for a crystalline sample obtained by this two-layer diffusion technique are given in Table I.

Microcrystalline samples of the mixed-valence $Mn^{II}Mn^{III}$ complexes $[LMn_2Cl_2Br]\cdot H_2O$ (**2**) and $[LMn_2Br_3]\cdot{}^1/_2CH_2Cl_2$ (**3**) were prepared by aerobically oxidizing the Mn^{II}_2 complexes with bromine water in a manner analogous to that used by Hoskins et al.[24] to prepare $Co^{II}Co^{III}$ Robson-type complexes. To a yellow solution containing 0.14 g (2.0 mmol) of $[LMn_2Cl_2]\cdot{}^1/_2CH_3OH$ [or 0.16 g of $[LMn_2Br_2]\cdot{}^1/_2CH_3OH$] in 300 mL of CH_2Cl_2 at room temperature was added bromine water (~2 mmol). The resulting solution slowly turned to a dark brownish green color. It was then boiled at atmospheric pressure to vaporize some of the CH_2Cl_2. At the point when a solid just started to precipitate from the solution, the solution was then cooled and a dark brownish green crystalline solid was obtained. Analytical data for **2** and **3** are given in Table I.

The crystal of $[LMn_2Cl_2Br]\cdot H_2O$ (**2**) used in the structure determination was grown by means of a two-layer diffusion technique. Toluene was layered over the top of a CH_2Cl_2 solution of $[LMn_2Cl_2Br]\cdot H_2O$ (**2**) and after several days X-ray quality crystals of **2** grew.

Physical Measurements. Variable-temperature, solid-state magnetic susceptibility data were measured with a series 800 VTS-50 SQUID susceptometer (S.H.E. Corp.) maintained by the Physics Department at the University of Illinois. The susceptometer was operated at a magnetic field strength of 10 kG. Diamagnetic corrections were estimated from Pascal's constants and subtracted from the experimental susceptibility data to obtain the molar paramagnetic susceptibilities of the compounds. These molar paramagnetic susceptibilities were fit to the appropriate theoretical expressions by means of a least-squares-fitting computer program.[25]

EPR spectra were recorded with either a Bruker ER200D X-band spectrometer or a Varian E15 Q-band spectrometer. Both spectrometers are housed in the National Biomedical ESR center at the University of Illinois. Frozen glass samples were prepared by dissolving the compounds in spectroscopic grade solvents. The solutions were frozen at liquid-nitrogen temperature as soon as possible after preparation. In independent experiments it was found that whether or not O_2 was pumped from the EPR tube before freezing and sealing did not affect the appearance of the spectra obtained.

Structure Determination on $Mn_2(C_{30}H_{38}N_4O_2)Cl_2$, LMn_2Cl_2 (4). A crystal suitable for crystallographic analysis was mounted on a glass fiber and examined for quality by using rotational and axial photographs and peak profiles after alignment on a Nicolet P3 automated diffractometer. Information regarding the structure determination is given in Table II. Three check reflections measured after every 97 reflections showed only statistical variations in intensity. An empirical absorption correction was applied to the data. The locations of Mn, O, Cl, two N atoms, and several carbon atoms were obtained by direct methods with SHELXTL; the remaining atoms were determined from difference Fourier maps generated by least-squares refinement of the atoms above. The molecule was found to be located about an inversion center at $^1/_2$, 0, 1. In the final refinement the *tert*-butyl group was refined as an idealized tetradron about the tertiary carbon atom with a C–C bond length of 1.524 Å. Although all hydrogen atoms were resolved, fixed contributions were included assuming idealized positions and C–H bond lengths of 0.96 Å. The largest parameter shift in the final cycle of refinement occurred for the rotational vector of C12 in the *tert*-butyl group with a change of 0.633 relative to its esd. The greatest residual electron density was found to be near C14 of the propyl bridging group with a value of 0.72 $e^-/Å^3$. Final atomic coordinates are given in Table III; tables containing anisotropic thermal parameters and structure factors are available as supplementary material.

Table II. Crystal Data and Details of the Structure Determinations on $[LMn_2Cl_2]$ and on $[LMn_2Cl_2Br]\cdot H_2O$

Crystal Data		
formula	$Mn_2C_{30}H_{38}O_2N_4Cl_2$	$Mn_2C_{30}H_{40}N_4O_3Cl_2Br$
mol wt	667.44	765.34
space group[a]	$P\bar{1}$	$C2/c$
crystal system	triclinic	monoclinic
a (Å)[b]	7.270 (1)	21.064 (7)
b (Å)	9.457 (2)	13.559 (4)
c (Å)	12.316 (2)	27.652 (6)
α (deg)	108.36 (1)	90.0
β (deg)	94.92 (1)	105.51 (2)
γ (deg)	99.58 (1)	90.0
V (Å^3)	783.8 (2)	7609.3
Z	1	8
d_{calcd} (g cm^{-3})	1.41	1.34
d_{exptl} (g cm^{-3})	1.39 (2)	1.38 (2)
$F(000)$	346	3127
μ (cm^{-1})	9.77	18.51
cryst size (mm)	0.20 × 0.13 × 0.13	0.32 × 0.24 × 0.34
Data Collection and Reduction		
data collected	$+h,\pm k,\pm l$	$+h,+k,\pm l$
scan range (2θ), min–max (deg)	3.0–50.0	3.0–40.0
scan (below Kα_1, above Kα_2) (deg)	0.9, 0.9	1.0, 1.0
unique reflcns measured	2769	4380
obsd reflcns	1884	1732
transmission factors	0.958–0.891	0.554–0.434
diffractometer	Nicolet P3F	Nicolet P3F
radiation (Å)	Mo Kα(0.71069)	Mo Kα(0.71069)
monochromator angle (deg)	12.2	12.2
temperature (K)	294–296	294–296
scan technique	θ–2θ	θ–2θ
variable scan speed (deg/min)	4.0 to 30.0	4.0 to 30.0
background	stationary crystal-stationary counter	stationary crystal-stationary counter
background time	0.5 (scan time)	0.5 (scan time)
criterion	$F > 6\sigma(F)$	$F > 6\sigma(F)$
absorption correction	empirical	empirical
Structure Determination and Refinement		
programs		SHELXTL[c]
scattering factors		neutral atoms[d]
R_1 and R_2[e]	0.0501, 0.0697	0.0711, 0.0974
weight	$1/(\sigma(F)^2 + 0.0017F^2)$	$1/(\sigma(F)^2 + 0.0051F^2)$
parameters	191	315
observations/parameters	9.8	5.5
GOF	1.319	1.206

[a] *International Tables for X-ray Crystallography*; Kynoch Press: Birmingham, England, 1965; Vol. 1. [b] Cell dimensions were determined by least-squares fit of the setting angles of 20 reflections with 2θ in the range 20–30°. [c] G. M. Sheldrick, SHELXTL, A Program for Crystal Structure Determination, Nicolet Instrument Corp., P.O. Box 4370, Madison, WI 53711-0508. [d] *International Tables for X-ray Crystallography*; Kynoch Press: Birmingham, England, 1974; Vol. 4, pp 55–60, 99–101, 149–150. [e] The quantity minimized in the least-squares procedures is $\sum w(|F_o| - |F_c|)^2$. $R_1 = \sum||F_o| - |F_c||/\sum|F_o|$. $R_2 = [\sum w(|F_o| - |F_c|)^2/\sum w(F_o)^2]^{1/2}$.

(23) Pilkington, N. H.; Robson, R. *Aust. J. Chem.* **1970**, *23*, 2225.
(24) Hoskins, B. F.; Robson, R.; Williams, G. A. *Inorg. Chim. Acta* **1976**, *16*, 121–133.
(25) Chandler, J. P., Program 66 of the Quantum Chemistry Program Exchange, Indiana University, Bloomington, IN.

Table III. Atomic Coordinates ($\times 10^4$) and Isotropic Thermal Parameters (Å, $\times 10^3$) for $[LMn_2Cl_2]$

	x	y	z	U[a]
Mn	4324 (1)	1617 (1)	10646 (1)	33 (1)
Cl	6374 (2)	3667 (2)	12072 (1)	52 (1)
O	5525 (5)	532 (4)	9181 (3)	37 (1)
N1	8239 (7)	-1333 (5)	8596 (4)	49 (2)
N2	3053 (6)	2673 (5)	9518 (4)	40 (2)
C1	6041 (7)	1043 (5)	8345 (4)	35 (2)
C2	5176 (8)	2132 (5)	8053 (4)	38 (2)
C3	5714 (8)	2624 (6)	7137 (4)	44 (2)
C4	7101 (7)	2127 (5)	6502 (4)	45 (2)
C5	7972 (8)	1095 (6)	6833 (5)	49 (2)
C6	7470 (7)	528 (6)	7720 (4)	40 (2)
C7	3709 (8)	2822 (6)	8622 (4)	40 (2)
C8	8529 (7)	-563 (6)	7920 (5)	45 (2)
C9	7688 (6)	2598 (4)	5486 (3)	59 (3)
C10	7183 (10)	1221 (7)	4381 (4)	97 (4)
C11	9810 (8)	3215 (9)	5705 (5)	138 (6)
C12	6660 (12)	3828 (8)	5359 (6)	169 (8)
C13	1576 (9)	3555 (7)	9905 (5)	55 (3)
C14	934 (16)	3456 (13)	10937 (10)	158 (8)
C15	440 (11)	2339 (9)	11348 (8)	88 (4)

[a] All atoms were refined with anisotropic thermal parameters. The equivalent isotropic U is defined as one-third of the trace of the orthogonalized U_{ij} tensor.

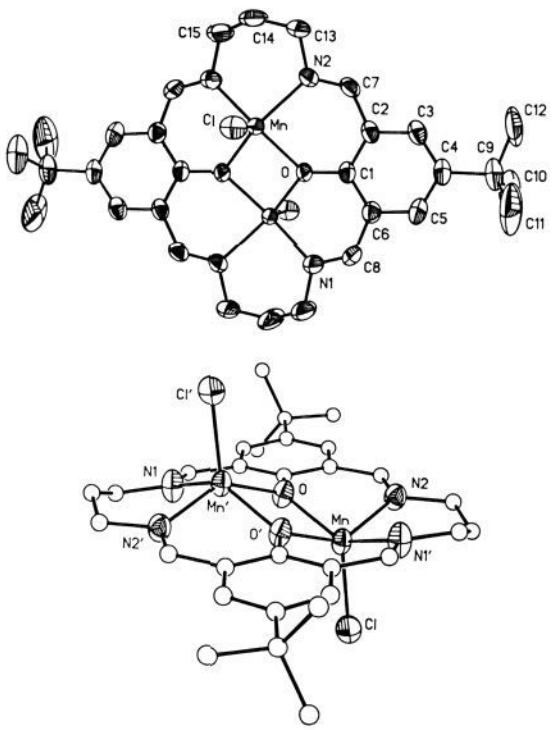

Figure 1. (Upper) ORTEP plot showing the planar structure of LMn_2Cl_2 (**4**). (Lower) View from the side of LMn_2Cl_2 (**4**) showing the displacement of the manganese atoms from the plane of the macrocyclic ligand.

Structure Determination on $Mn_2(C_{30}C_{38}N_4O_2)Cl_2Br\cdot H_2O$, $[LMn_2Cl_2Br]\cdot H_2O$ (2). A crystal suitable for crystallographic analysis was mounted on a glass fiber and examined for quality by using rotational and axial photographs and peak profiles after alignment on a Nicolet P3 automated diffractometer. Information regarding the structure determination is in *Table II. Three check reflections measured after every 97 reflections* showed no significant decreases in intensity. An empirical absorption correction was applied to the data. Locations of the two Mn atoms were obtained by direct methods with SHELXTL; the remaining atom positions were determined from the phases generated by least-squares refinement of the positions of the two metal atoms. A number of disorder problems were encountered during the structure determination. The terminally bonded halogen atoms were refined as 0.3 Cl/0.7 Br at the position labeled Br in the figures, and 0.3 Br/0.7 Cl at the Cl1 position. Carbon C29 of the propylene bridge was found to be disordered with half occupancy on either side of the macrocycle plane, and the *tert*-butyl group centered at C9 suffered from twofold disorder with half occupancy for the two sets of carbon atoms. Residual electron density on the final difference Fourier at the position indicated as O3 in the table of atom parameters was identified analytically as a fractional water solvate molecule. This position is close to a crystallographic inversion center and may reflect random occupancy on either site but not both simultaneously. Fixed contributions for hydrogen atoms were included assuming idealized positions and a C–H bond length of 0.96 Å. The largest parameter shift on the final cycle of refinement occurred for the thermal parameter of the *tert*-butyl carbon, C12′, with a change of 0.450 relative to its esd. The greatest residual electron density was near the bridging halogen, Cl2, with a value of 0.75 $e^-/Å^3$. Final atomic coordinates are given in Table IV; tables containing anisotropic thermal parameters and structure factors are available as supplementary material.

Table IV. Atomic Coordinates ($\times 10^4$) and Isotropic Thermal Parameters (Å, $\times 10^3$) for $[LMn_2Cl_2Br]\cdot H_2O$

	x	y	z	U
Mn1	3271 (1)	6814 (2)	2279 (1)	68 (1)[a]
Mn2	3230 (1)	8017 (2)	1288 (1)	64 (1)[a]
Br/Cl1	4021 (1)	8485 (2)	788 (1)	54 (3)[a,b]
Cl1/Br	2528 (2)	7325 (2)	2799 (1)	87 (5)[a,c]
Cl2	3974 (2)	6340 (3)	1597 (2)	84 (2)[a]
O1	2631 (5)	6829 (7)	1627 (3)	69 (5)[a]
O2	3454 (5)	8130 (7)	2084 (4)	72 (5)[a]
N1	2320 (6)	7886 (9)	688 (4)	64 (6)[a]
N2	2951 (6)	9585 (9)	1376 (4)	65 (6)[a]
N3	3103 (7)	5423 (9)	2412 (5)	81 (6)[a]
N4	4096 (6)	6870 (10)	2862 (5)	88 (7)[a]
C1	2362 (7)	6075 (12)	1356 (5)	54 (4)
C2	2046 (7)	6163 (10)	847 (5)	49 (4)
C3	1716 (7)	5381 (11)	565 (6)	65 (5)
C4	1722 (8)	4436 (12)	771 (6)	67 (5)
C5	2055 (8)	4303 (13)	1258 (7)	80 (5)
C6	2389 (8)	5139 (12)	1552 (6)	70 (5)
C7	1971 (7)	7079 (11)	575 (5)	56 (4)
C8	2703 (8)	4833 (13)	2076 (6)	77 (5)
C9	1363 (9)	3557 (14)	453 (7)	86 (6)
C10	1059 (41)	3917 (42)	-74 (17)	214 (55)[d]
C11	1147 (21)	2824 (27)	817 (15)	130 (23)[d]
C12	1914 (23)	3001 (36)	318 (21)	171 (31)[d]
C10′	646 (15)	3835 (22)	287 (12)	76 (15)[d]
C11′	1439 (23)	2535 (21)	745 (13)	129 (23)[d]
C12	1469 (34)	3508 (33)	-59 (16)	138 (33)[d]
C13	3740 (7)	8870 (11)	2402 (5)	57 (4)
C14	4194 (7)	8691 (12)	2862 (6)	64 (5)
C15	4510 (8)	9430 (13)	3175 (6)	78 (5)
C16	4335 (8)	10413 (13)	3034 (6)	76 (5)
C17	3867 (7)	10596 (12)	2581 (6)	64 (5)
C18	3592 (7)	9835 (11)	2251 (5)	56 (4)
C19	3177 (7)	10129 (11)	1773 (5)	62 (5)
C20	4383 (8)	7710 (12)	3037 (6)	83 (6)
C21	4646 (8)	11278 (15)	3388 (7)	84 (6)
C22	4327 (17)	12156 (18)	3249 (10)	308 (25)[a]
C23	5345 (9)	11297 (18)	3441 (9)	163 (16)[a]
C24	4606 (12)	11021 (19)	3907 (8)	168 (16)[a]
C25	2144 (7)	8706 (11)	348 (5)	62 (7)[a]
C26	2003 (8)	9601 (13)	621 (5)	81 (9)[a]
C27	2593 (9)	10143 (12)	931 (6)	92 (9)[a]
C28	4382 (11)	5957 (18)	3115 (10)	177 (16)[a]
C29	4112 (17)	5140 (24)	3071 (11)	83 (16)[a,d]
C29′	3811 (19)	5416 (33)	3320 (15)	83 (14)[a,d]
C30	3366 (12)	4946 (13)	2903 (6)	104 (11)[a]
O3	163 (15)	9182 (41)	-49 (31)	127 (24)[a,d]

[a] Atoms refined with anisotropic thermal parameters. Equivalent isotropic U defined as one-third the trace of the orthogonalized U_{ij} tensor. [b] Atom refined as 0.7 Br and 0.3 Cl. [c] Atom refined as 0.7 Cl and 0.3 Br. [d] Atom refined with an occupancy factor of 0.5.

Results and Discussion

X-ray Structure of LMn_2Cl_2 (4). For comparison purposes it was desirable to have the X-ray structure of one of the binuclear Mn^{II}_2 complexes. Drawings showing the centrosymmetric complex molecule are given in Figure 1; bond distances and angles are given in Table V. The macrocyclic ligand in **4** is essentially planar, the only significant deviations from planarity occur for the phenyl rings which are rotated approximately 4.0° from the N_4O_2 plane. The Mn atoms are displaced by 0.69 Å on either side of the ligand

Table V. Selected Bond Lengths and Angles for $[LMn_2Cl_2]$

	Bond Lengths (Å)		
Mn–Cl	2.348 (1)	C1–C2	1.412 (8)
Mn–O	2.114 (3)	C1–C6	1.406 (8)
Mn–O′	2.128 (4)	C2–C3	1.411 (8)
Mn–N1	2.169 (5)	C3–C4	1.382 (8)
Mn–N2	2.177 (5)	C2–C7	1.458 (8)
Mn–Mn′	3.324 (4)	C4–C5	1.390 (9)
C1–O	1.325 (7)	C5–C6	1.409 (9)
C8–N1	1.276 (9)	C6–C8	1.453 (9)
C15′–N1	1.472 (11)	C13–C14	1.415 (15)
C7–N2	1.277 (8)	C14–C15	1.321 (17)
C13–N2	1.487 (8)		
	Bond Angles (deg)		
Mn–O–Mn′	103.2 (2)	Mn′–N1–C8	124.4 (4)
Cl–Mn–O	115.2 (1)	Mn′–N1–C15′	118.1 (5)
Cl–Mn–N1′	104.2 (1)	C8–N1–C15′	116.2 (6)
Cl–Mn–O′	113.4 (1)	Mn–N2–C7	124.0 (4)
O–Mn–O′	76.8 (2)	Mn–N2–C13	119.5 (4)
O–Mn–N1′	140.2 (1)	C7–N2–C13	115.3 (5)
O′–Mn–N1′	83.1 (2)	O–C1–C2	121.0 (5)
O′–Mn–N2	142.6 (1)	O–C1–C6	121.4 (5)
N2–Mn–Cl	103.8 (1)	C1–C6–C8	124.9 (5)
O–Mn–N2	84.4 (2)	N1–C8–C6	127.5 (5)
N1′–Mn–N2	91.6 (2)	N2–C7–C2	128.2 (6)
Mn–O–C1	128.9 (3)	C1–C2–C7	125.4 (5)
Mn′–O–C1	127.9 (3)		

plane. Average Mn–O and Mn–N lengths of 2.121 (4) and 2.173 (5) Å are on the shorter side of values typically found for Mn^{II}.[26-30] Displacement of the metal ions off the ligand plane is clearly due to the large radius of the metal ion coupled with the in-plane bonding constraints of the macrocycle. Hoskins et al.[31] reported structural characterization of the Co^{II}_2 analogue of this complex differing in substituent (methyl groups rather than the *tert*-butyl groups in the present case) and bromo rather than chloro ligands. The smaller radius of Co^{II} (0.81 Å) relative to Mn^{II} (0.89 Å) results in Co–O and Co–N lengths that are shorter than those of the Mn structure by approximately 0.08 Å and a displacement of the Co^{II} ions from the ligand plane by only 0.30 Å. The binuclear Cu^{II} analogue with a still shorter radius (0.79 Å) has metal ions only 0.21 Å out of the plane.[32] This dependence upon metal ion radius appears in other features of the macrocycle structures with a consistent increase in M–M separation, from 3.133 Å for $Cu^{II}\cdots Cu^{II}$ to 3.158 and 3.324 Å for $Co^{II}\cdots Co^{II}$ and $Mn^{II}\cdots Mn^{II}$, respectively, and ligand O--O separation, from 2.42 to 2.56 and 2.64 Å, for the Cu, Co, Mn series. It is of interest that in the present structure determination none of the disorder and space group ambiguity found with structures on complexes prepared with the methyl-substituted ligand was encountered.

Synthesis of $Mn^{II}Mn^{III}$ Complexes. We have found that the oxidation of a binuclear Mn^{II}_2 complex such as LMn_2Cl_2 (**4**) to give a $Mn^{II}Mn^{III}$ complex must be performed with a stoichiometric amount of bromine water. If too much bromine water is added, products of composition $LMn_2Cl_2Br_x$ ($1 < x < 3$) are obtained instead of LMn_2Cl_2Br or LMn_2Br_3. Neither LMn_2Cl_2Br nor LMn_2Br_3 has been isolated successfully from $LMn_2Cl_2Br_x$. If too little bromine water is added, the oxidation of LMn_2Cl_2 to give LMn_2Cl_2Br is not complete and a mixture results. Furthermore, in the synthetic approach described in this paper control on the evaporation of the CH_2Cl_2/bromine water solution has to be exercised; otherwise CH_2Cl_2 or bromine will be lost too fast to get a stoichiometric oxidation. When the oxidation is not complete, the Mn^{II}_2 and $Mn^{II}Mn^{III}$ complexes could be separated by extracting the latter into methanol. The nature of the $LMn_2Cl_2Br_x$ solids remains to be determined.

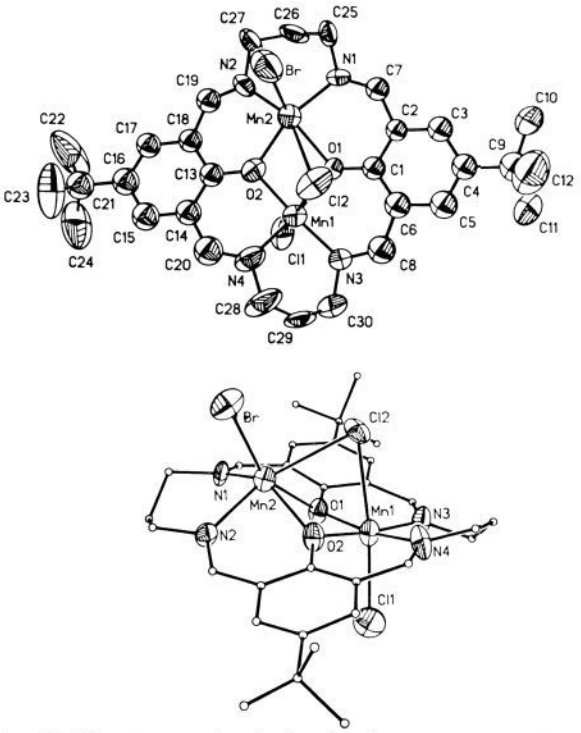

Figure 2. (Upper) ORTEP plot showing the planar structure of $[LMn_2Cl_2Br]\cdot H_2O$ (**2**) and the distorted trigonal prismatic coordination geometry of Mn2. (Lower) View showing the disposition of the manganese atoms with respect to the plane of the macrocyclic ligand of $[LMn_2Cl_2Br]\cdot H_2O$ (**2**).

Table VI. Selected Bond Lengths and Angles for $[LMn_2Cl_2Br]\cdot H_2O$[a]

	Bond Lengths (Å)		
Mn1–Cl1	2.491 (5)	Mn1–Cl2	2.766 (6)
Mn1–O1	1.941 (9)	Mn1–O2	1.931 (10)
Mn1–N3	1.973 (13)	Mn1–N4	2.031 (12)
Mn2–Br	2.514 (4)	Mn2–Cl2	2.763 (5)
Mn2–O1	2.386 (11)	Mn2–O2	2.129 (10)
Mn2–N1	2.182 (11)	Mn2–N2	2.236 (17)
O1–C1	1.31 (2)	O2–C13	1.36 (2)
N1–C7	*1.31 (2)*	*N1–C25*	*1.44 (2)*
N2–C19	1.30 (2)	N2–C27	1.47 (2)
N3–C8	1.34 (2)	N3–C30	1.47 (2)
N4–C20	1.32 (2)	N4–C28	1.47 (3)
Mn1–Mn2	3.168 (3)		
	Bond Angles (deg)		
Cl1–Mn1–Cl2	172.6 (1)	Cl1–Mn1–O1	98.4 (4)
Cl2–Mn1–O1	74.6 (4)	Cl1–Mn1–O2	96.1 (4)
Cl2–Mn1–O2	80.9 (4)	O1–Mn1–O2	82.7 (4)
Cl1–Mn1–N3	89.2 (5)	Cl2–Mn1–N3	93.4 (5)
O1–Mn1–N3	93.9 (4)	O2–Mn1–N3	174.0 (5)
Cl1–Mn1–N4	93.9 (5)	Cl2–Mn1–N4	92.9 (5)
O1–Mn1–N4	166.2 (6)	O2–Mn1–N4	89.7 (5)
N3–Mn1–N4	92.6 (5)	Br–Mn2–Cl2	88.5 (1)
Br–Mn2–O1	152.1 (3)	Cl2–Mn2–O1	68.8 (3)
Br–Mn2–O2	123.7 (3)	Cl2–Mn2–O2	77.9 (3)
O1–Mn2–O2	68.7 (4)	Br–Mn2–N1	100.3 (4)
Cl2–Mn2–N1	118.5 (3)	O1–Mn2–N2	78.1 (4)
O2–Mn2–N1	134.3 (5)	Br–Mn2–N2	93.0 (4)
Cl2–Mn2–N2	153.2 (3)	O1–Mn2–N2	114.7 (4)
O2–Mn2–N2	79.1 (4)	N1–Mn2–N2	87.5 (4)
Mn1–Cl2–Mn2	69.9 (1)	Mn1–O1–Mn2	93.6 (4)
Mn1–O2–Mn2	102.5 (4)		

[a] Atoms listed as Br and Cl1 are 0.7 Br/0.3 Cl1 and 0.7 Cl1/0.3 Br, respectively.

X-ray Structure of $[LMn_2Cl_2Br]\cdot H_2O$ (2). Views of $[LMn_2Cl_2Br]$ are given in Figure 2; bond distances and angles are given

(26) Lynch, M. W.; Hendrickson, D. N.; Fitzgerald, B. J.; Pierpont, C. G. *J. Am. Chem. Soc.* **1984**, *106*, 2041–2049.
(27) Boucher, L.; Day, V. *Inorg. Chem.* **1977**, *16*, 1360–1366.
(28) McKee, V.; Shepard, W. *J. Chem. Soc., Chem. Commun.* **1985**, *3*, 158–159.
(29) Drew, M.; Hamid bin Othman, A.; McFall, S. G.; McIlroy, P. D. A.; Martin-Nelson, S. *J. Chem. Soc., Dalton Trans.* **1977**, 1173–1180.
(30) Mabad, B.; Cassoux, P.; Tuchagues, J.-P.; Hendrickson, D. N. *Inorg. Chem.* **1986**, *25*, 1420–1431.
(31) Hoskins, B. F.; Williams, G. A. *Aust. J. Chem.* **1975**, *28*, 2607–2614.
(32) Hoskins, B. F.; McLeod, N. J.; Schapp, H. A. *Aust. J. Chem.* **1976**, *29*, 515–521.

in Table VI. In a previous section we pointed out that metal ion radius played an important role in determining the structural features of the macrocycle complex. The ionic radii of Mn^{II} and Mn^{III} ions differ significantly, and it has been established that in tetragonally coordinated complexes equatorial Mn–O and Mn–N lengths can be 0.2 Å shorter for Mn^{III} than for Mn^{II}.[33,34] This large difference is clearly apparent in the structure of **2** and permits differentiation between ions of different oxidation state; atom Mn1 in Figure 2 is the Mn^{III} ion, while Mn2 is the Mn^{II} ion. The average Mn1–O length is 1.936 (10) Å compared with values of 2.129 (10) and 2.386 (11) Å to Mn2. A similar difference can be seen for the Mn–N lengths in Table VI. With a smaller radius Mn1 lies 0.15 Å out of the O1, O2, N3, N4 least-squares plane, toward chloride Cl1. The Mn2 ion sits atop the O1, O2, N1, N2 plane, displaced from this plane by 1.25 Å toward the halogen ligands. Macrocycle donor atoms N2, O1, O2, N3, N4 form a well-defined plane with average deviations of 0.06 Å. Nitrogen N1 lies 1.00 Å off this plane, toward Mn2. This distortion of the ligand plane is further reflected in the 17.9° dihedral angle between planes of the phenolic rings. The nitrogen and oxygen donor atoms bonded to Mn2 approximately define the square face of a trigonal prismatic coordination polyhedron. The bridging chlorine ligand Cl2 occupies an additional site of the trigonal prism, although both Mn–Cl2 lengths are quite long [2.763 (5), 2.766 (6) Å]. The terminally bound halogen, Br, is located at a position bent toward nitrogen N2, relative to the site it might occupy for a regular trigonal prismatic geometry. This distortion, with displacement of N1 from the macrocycle plane, appears to represent a twist of the N1, N2, Br face of the coordination polyhedron toward an octahedral geometry. This unusually large displacement of Mn2 from the ligand plane, relative to the displacement found in the LMn_2Cl_2 (**4**) structure, appears to result from the preference of Mn1 for an in-plane site, while maintaining a Mn1–Mn2 separation which is consistent with the ionic radii. This separation is 3.168 (3) Å. It is of interest to compare this result with the two $Co^{II}Co^{III}$ structures reported by Hoskins with the methyl analogue of this ligand.[24,35] In these two cases the difference in ionic radii is less, the Co^{III} ions lie in the macrocycle plane, and the Co^{II} ions lie slightly off the plane (0.067, 0.096 Å). The Co–Co separation is 3.13 Å, and the coordination polyhedra are more regular octahedra.

Electrochemisty of Mn^{II}_2 Complexes. In view of the above comments about the preparation of $Mn^{II}Mn^{III}$ complexes by oxidation with bromine water, it was of interest to determine the redox properties of LMn_2Cl_2 and LMn_2Br_2. Information about the relative stability of the mixed-valence $Mn^{II}Mn^{III}$ complex can also be gleaned from the electrochemical data.

In Figure 3 are shown the cyclic voltammograms that result from oxidizing 1:1 CH_3CN/CH_2Cl_2 solutions of $[LMn_2Cl_2]\cdot{}^1/_2CH_3OH$ and $[LMn_2Br_2]\cdot{}^1/_2CH_3OH$. In the former case the CV exhibits two waves, one at $E^1_{1/2}$ = +0.596 V (vs. NHE) with a peak-to-peak separation of 178 mV and the other at $E^2_{1/2}$ = +1.20 V with a peak-to-peak separation of 140 mV. The first wave is likely due to a one-electron oxidation to give $LMn_2Cl_2^+$, followed by the second wave where the $LMn^{III}_2Cl_2^{2+}$ complex is formed. For comparison purposes it should be noted that $[LCu^{II}_2]BF_4$ in DMF exhibits two one-electron reduction waves at $E^1_{1/2}$ = –0.534 V and $E^2_{1/2}$ = –0.927 V with peak-to-peak separations of 72 and 73 mV, respectively.[36,37] Thus, either the CH_3CN/CH_2Cl_2 solvent choice for the Mn^{II}_2 complexes at a glass carbon electrode is not as good as DMF for $[LCu^{II}_2]BF_4$ at a Pt electrode or the waves observed for the Mn^{II}_2 complexes are not as reversible as those observed for the Cu^{II}_2 complex. From the

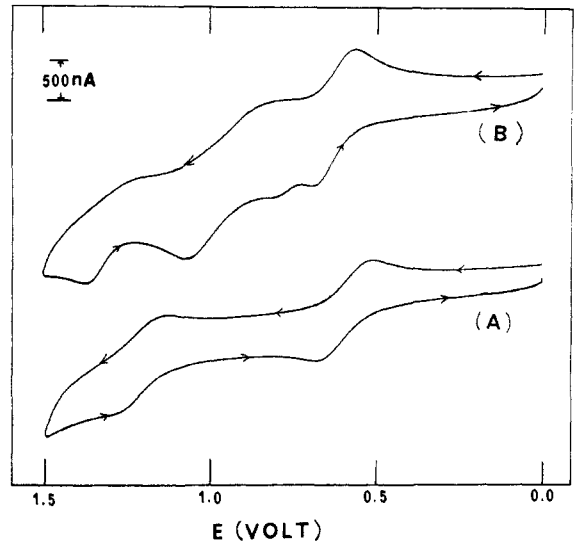

Figure 3. Cyclic voltammograms for (A) $[LMn_2Cl_2]\cdot{}^1/_2CH_3OH$ (0.28 mM) and (B) $[LMn_2Br_2]\cdot{}^1/_2CH_3OH$ (0.31 mM) dissolved in 1:1 CH_3CN/CH_2Cl_2 with 0.1 M $[(n\text{-}Bu)_4N]ClO_4$. The scan rate was 20 mV/s with a glassy carbon electrode. The potentials are referenced to a NHE. The IR drop has been compensated automatically by the instrument (BAS100).

EPR studies of LMn_2Cl_2Br (vide infra) it is known that there is some appreciable change in this mixed-valence $Mn^{II}Mn^{III}$ complex in DMF compared to a less polar solvent; as a consequence, DMF could not be used for the Mn^{II}_2 electrochemistry.

Examination of Figure 3 shows that $[LMn_2Br_2]\cdot{}^1/_2CH_3OH$ in CH_3CN/CH_2Cl_2 exhibits a more complicated electrochemistry than $[LMn_2Cl_2]\cdot{}^1/_2CH_3OH$. At least three redox waves and perhaps even some other chemistry are evident. The waves for oxidation of LMn_2Br_2 to $LMn_2Br_2^{2+}$ fall at $E^1_{1/2}$ = +0.629 V and $E^2_{1/2}$ = +1.3 V with peak-to-peak separations of ~132 and ~140 mV, respectively. The third wave at ca. +0.9 V is probably attributable to $Br^- \rightleftharpoons {}^1/_2Br_2(aq) + e^-$, which is reported[38] to occur at $E_{1/2}$ = +1.087 V vs. NHE.

The stability of a mixed-valence $Mn^{II}Mn^{III}$ complex can be judged by its conproportionation constant, K_{con}, for the following equilibrium:

$$[LMn^{III}_2X_2]^{2+} + LM^{II}_2X_2 \overset{K_{con}}{\rightleftharpoons} 2[LMn^{II}Mn^{III}X_2]^+$$

$$E^1_{1/2} - E^2_{1/2} = -0.0591 \log (K_{con})$$

From the above electrochemical data K_{con} is calculated to be 1.7×10^{10} for LMn_2Cl_2 and 2.3×10^{11} for LMn_2Br_2. Obviously the mixed-valence forms of these two complexes are quite stable. It is interesting that $K_{con} = 4.3 \times 10^6$ for the following equilibrium:[36,37]

$$[LCu^{II}_2]^{2+} + LCu^{I}_2 \overset{K_{con}}{\rightleftharpoons} 2[LCu^{I}Cu^{II}]^+$$

Furthermore, for a series of 12 different $[LCu^{II}_2]^{2+}$ complexes with various Robson-type ligands (i.e., different diamine linkages) it was found[37] that K_{con} varies from 3.1×10^5 to 7.1×10^8. Thus, the mixed-valence $[LMn^{II}Mn^{III}X_2]^+$ complexes are more stable to disproportionation than are the various mixed-valence $[LCu^{I}Cu^{II}]^+$ complexes. Several factors may contribute to this. Perhaps the differences in ligation and coordination geometry preferences between Cu^{II} and Cu^{I} ions exceed those between Mn^{III} and Mn^{II} ions. A tendency to become involved in a Jahn–Teller distortion is present in one ion of both pairs, $Mn^{II}Mn^{III}$ or $Cu^{I}Cu^{II}$. The greater covalency in metal–ligand interactions in the copper complexes is probably involved in determining the relative stabilities of mixed-valence states versus same-valence states.

The comparison between $[LCu^{I}Cu^{II}]^+$ and $[LMn^{II}Mn^{III}X_2]^+$ brings out the interesting question of when and whether the va-

(33) Larsen, S. K.; Pierpont, C. G.; DeMunno, G.; Dolcetti, G. *Inorg. Chem.* **1986**, *25*, 4828–4831.
(34) Davies, J.; Gatehouse, B.; Murray, K. *J. Chem. Soc. Dalton* **1973**, 2523–2527.
(35) Hoskins, B. F.; Williams, G. A. *Aust. J. Chem.* **1975**, *28*, 2593–2605.
(36) Long, R. C.; Hendrickson, D. N. *J. Am. Chem. Soc.* **1983**, *105*, 1513–1521.
(37) Hendrickson, D. N.; Long, R. C.; Hwang, Y. T.; Chang, H.-R. In *Biological & Inorganic Copper Chemistry*; Karlin, K. D., Zubieta, J., Eds.; Adenine: Guilderland, NY, 1986.
(38) Latimer, W. M. *The Oxidation States of the Elements and Their Potentials in Aqueous Solution*, 2nd ed.; Prentice-Hall: New York, 1952.

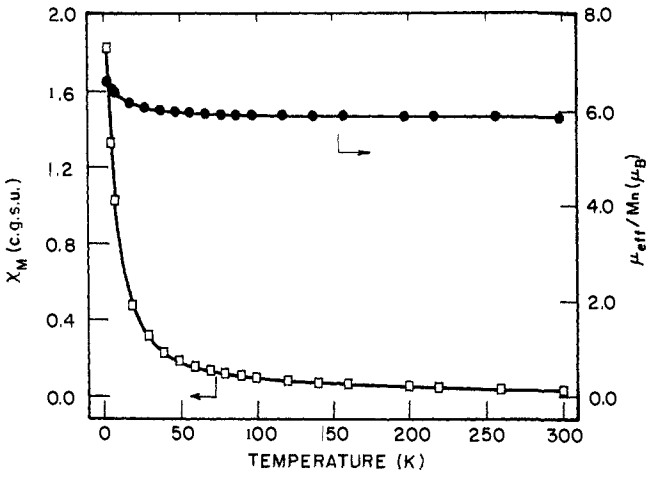

Figure 4. Plots of the molar paramagnetic susceptibility per binuclear complex, χ_M, versus temperature and of the effective magnetic moment per manganese ion, μ_{eff}/Mn, versus temperature for LMn_2Cl_2 (**4**). The solid lines represent the least-squares fit of the χ_M versus temperature data to the theoretical equation resulting from an isotropic exchange interaction. See text for parameters.

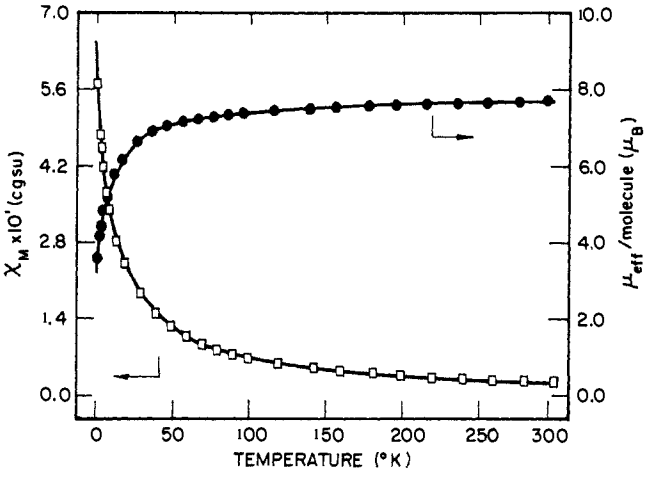

Figure 5. Plots of the molar paramagnetic susceptibility per molecule, χ_M, versus temperature and of the effective magnetic moment per molecule, μ_{eff}, versus temperature for $[LMn_2Cl_2Br]\cdot H_2O$ (**2**). The solid lines illustrate the quality of the two best fits of the χ_M data to the full-matrix diagonalization approach including single-ion zero-field splitting. See the text for parameters.

lences in these mixed-valence manganese complexes can become detrapped. EPR data for the series of 12 $[LCu^{I}Cu^{II}]^+$ complexes with different Robson L ligands show that certain complexes transfer electrons faster than the EPR time scale at room temperature in solution, whereas others are valence trapped on the EPR time scale.[36,37] Thus, certain of the $[LCu^{I}Cu^{II}]^+$ complexes give a room temperature solution EPR spectrum with 7 copper hyperfine lines (valence detrapped) while the spectrum for others exhibits only 4 copper hyperfine lines (valence trapped). The absence of any EPR signal for a room temperature solution of either $LMn^{II}Mn^{III}Cl_2Br$ or $LMn^{II}Mn^{III}Br_3$ may be evidence for relatively valence-trapped ions in these complexes. The valence trapping for these complexes likely reflects the appreciable difference in coordination geometry between the Mn^{II} and Mn^{III} ions in each complex. Only one mixed-valence manganese complex, μ_3-oxo-bridged $[Mn_3O(O_2CCH_3)_6(py)_3](py)$ where py is pyridine, has been shown[39,40] to become valence-detrapped. At ~185 K there is first-order phase transition,[41] above which this Mn_3O complex experiences an increase in its intramolecular rate of electron transfer.

Magnetic Susceptibility Studies. The magnitude of the intramolecular magnetic exchange interaction in a binuclear Mn^{II}_2 or $Mn^{II}Mn^{III}$ complex affects the rate of inter-ion electron exchange and electron transfer, respectively, and also the appearance of the EPR spectra for these two types of complexes. For example, there is still the question of why only the S_2 state, not the S_0 state, of PSII gives rise to an EPR signal.[4] It is believed that the S_2 state cluster has a $Mn^{III}_3Mn^{IV}$ oxidation state and the S_0 state would then have an $Mn^{III}_3Mn^{II}$ oxidation state content. Both are obviously odd-spin mixed-valence Mn_4 complexes which should be EPR active.

Magnetic susceptibility data were collected in the range 6.0–300.7 K for a microcrystalline sample of $[LMn_2Cl_2]\cdot {}^1/_2CH_3OH$. The data are given in the supplementary material and Figure 4, where it can be seen that the effective magnetic moment per Mn^{II} ion (μ_{eff}/Mn) gradually increases from 5.84 μ_B at 300.7 K to 6.00 μ_B at 40 K, and then increases appreciably to 6.59 μ_B at 6.0 K. There is clearly a weak ferromagnetic interaction between the two Mn^{II} ions in $[LMn_2Cl_2]\cdot {}^1/_2CH_3OH$. A similar weak ferromagnetic interaction has been noted[42] for $L'Mn_2Cl_2$, where $(L')^{2-}$ is the same as $(L)^{2-}$, except the *tert*-butyl substituent of $(L)^{2-}$ is replaced by a methyl group.

The susceptibility data for $[LMn_2Cl_2]\cdot {}^1/_2CH_3OH$ were least-squares fit to the simple theoretical susceptibility equation resulting from an isotropic magnetic exchange interaction between two $S_1 = S_2 = {}^5/_2$ ions as governed by the spin Hamiltonian $\hat{\mathbf{H}} = -2J\hat{\mathbf{S}}_1\cdot\hat{\mathbf{S}}_2$. This equation appears in a previous paper.[42] The solid lines in Figure 4 represent this least-squares fit which gives the parameters $J = +0.24$ cm^{-1} and $g = 1.97$ with the temperature independent paramagnetism (TIP) held constant at 200×10^{-6} cgsu per binuclear complex. The present value of J for $[LMn_2Cl_2]\cdot {}^1/_2CH_3OH$ compares favorably with $J = +0.20$ cm^{-1} reported[42] for $L'Mn_2Cl_2$. In fact, in this previous study it was found that the exchange interaction monotonically becomes more antiferromagnetic as the metal is varied across the series $L'Mn_2Cl_2$ from Mn^{II} ($J = +0.20$ cm^{-1}), to Fe^{II} (−4.2 cm^{-1}), to Co^{II} (−9.3 cm^{-1}), to Ni^{II} (−36.0 cm^{-1}), and finally to Cu^{II} (−294 cm^{-1}). This trend probably reflects three factors. In the series $Mn^{II}\cdots Cu^{II}$, the ionic radius is decreasing from Mn^{II} to Cu^{II}. The Cu^{II} ion fits best in the plane of the L′ (or L) ligand and this would increase antiferromagnetic interactions propagated by the phenoxide O atoms. Second, the covalency of the M–O bond increases in the series from Mn^{II} to Cu^{II} and this would increase the antiferromagnetic interaction. Finally, the number of unpaired electrons in t_{2g}-type (i.e., π-type) orbitals decreases from Mn^{II} to Cu^{II}. Unpaired electrons in t_{2g} orbitals introduce ferromagnetic exchange pathways. A net antiferromagnetic exchange interaction occurs for the series MnO, FeO, CoO, and NiO, each of which has a rock-salt structure.[43] It is relevant to note that the antiferromagnetic interaction increases monotonically in the series MnO, FeO, CoO, and NiO, and this trend has been explained[44] in terms of the second and third factors mentioned above.

Variable-temperature magnetic susceptibility data were also determined for $[LMn_2Cl_2Br]\cdot H_2O$ in the range 2.1–199.5 K and for $[LMn_2Br_3]\cdot {}^1/_2CH_2Cl_2$ in the range 2.9–299.2 K. Data for these two mixed-valence complexes are given in the supplementary material. As can be seen in Figure 5, the value of μ_{eff}/molecule for $[LMn_2Cl_2Br]\cdot H_2O$ decreases from 7.11 μ_B at 199.5 K to 2.36 μ_B at 2.1 K. When there is no magnetic exchange interaction present in such a binuclear $Mn^{II}Mn^{III}$ complex, the molar paramagnetic susceptibilities of the two different metal centers are

(39) For X-ray structures and magnetic susceptibility data see: Vincent, J. B.; Chang, H.-R.; Folting, K.; Huffman, J. C.; Christou, G.; Hendrickson, D. N. *J. Am. Chem. Soc.* **1987**, *109*, 5703–5711.

(40) Solid-state ^2H NMR spectra have been run for a single crystal of $[Mn_3O(O_2CCD_3)_6(ph)_3](py)$ at several temperatures above and below the phase transition at 185 K, see: Lowery, M. D.; Chang, H.-R.; Vincent, J. B.; Christou, G.; Hendrickson, D. N.; Wittebort, R. J., unpublished results.

(41) The heat capacity for this Mn_3O complex has been determined from 13 to 300 K, see: Sorai, M.; Vincent, J. B.; Christou, G.; Hendrickson, D. N., unpublished results.

(42) Lambert, S. L.; Hendrickson, D. N. *Inorg. Chem.* **1979**, *18*, 2683–2686.

(43) Anderson, P. W. *Phys. Rev.* **1950**, *79*, 350; **1959**, *115*, 2.

(44) Nesbet *Phys. Rev.* **1960**, *119*, 658.

added together to give the paramagnetic susceptibility for the binuclear complex. Consequently, the spin-only value of μ_{eff}/molecule for a binuclear $Mn^{II}Mn^{III}$ complex would be expected to be 7.68 μ_B in the absence of an exchange interaction. The presence of an antiferromagnetic exchange interaction in an $Mn^{II}Mn^{III}$ complex leads to an $S = {}^1/_2$ ground state with $S = {}^3/_2, {}^5/_2, {}^7/_2$, and ${}^9/_2$ excited states. From the measured value of μ_{eff}/molecule for $[LMn_2Cl_2Br]\cdot H_2O$ at 199.5 K it is clear there is a weak antiferromagnetic interaction present. The relatively abrupt decrease in μ_{eff}/molecule for $[LMn_2Cl_2Br]\cdot H_2O$ (see Figure 5) below ~50 K could be due either to the onset of Boltzmann depopulation of excited spin states or to the effects associated with single-ion, zero-field interactions on the Mn^{III} or the Mn^{II} ion.

The simplest analysis of the magnetic susceptibility data for $[LMn_2Cl_2Br]\cdot H_2O$ (fitting data are given in the supplementary material) involves only an isotropic magnetic exchange between an $S_1 = {}^5/_2$ Mn^{II} ion and an $S_2 = 2$ Mn^{III} ion as governed by $\hat{H} = -2J\hat{S}_1\cdot\hat{S}_2$. The expression for the molar paramagnetic susceptibility of a binuclear $Mn^{II}Mn^{III}$ complex is given in standard references.[45] We have found that least-squares fitting of the data for $[LMn_2Cl_2Br]\cdot H_2O$ in this manner gives $J = -1.8$ cm^{-1} and $g = 1.84$; however, this fit is not good.

In an effort to explicitly account for single-ion, zero-field splitting effects, a different theoretical model was devised. Two assumptions were made to make this model tractable. First, it was assumed that the **g** tensors on the two metal ions are collinear and that the resulting average **g** tensor is axial. Second, rhombic single-ion, zero-field splitting effects, which are expected to be small, were neglected. With these simplifications the spin Hamiltonian assumes the following form:

$$\hat{H} = g_{\parallel}\beta H_z\hat{S}_z + g_{\perp}\beta(H_x\hat{S}_x + H_y\hat{S}_y) + D_1[\hat{S}_{z1}^2 - {}^1/_3S_1(S_1+1)] + D_2[\hat{S}_{z2}^2 - {}^1/_3S_2(S_2+1)] - 2J\hat{S}_1\cdot\hat{S}_2 \quad (1)$$

In eq 1 D_1 and D_2 are the axial single-ion, zero-field splitting parameters for the Mn^{II} and Mn^{III} ions, respectively. Equation 1 can be used to obtain the magnetic susceptibility of a binuclear $Mn^{II}Mn^{III}$ complex by first deriving the 30 eigenfunctions, employing $3J$ coupling coefficients to write each coupled wave function $|S_1S_2SM_s\rangle$ as a product of uncoupled wave functions $|M_{S1}\rangle|M_{S2}\rangle$. These 30 coupled wave functions are given in the supplementary material together with all of the non-zero matrix elements of the 30 × 30 Hamiltonian energy matrix including the effects of magnetic exchange, zero-field splitting, and Zeeman interactions. The Hamiltonian matrix is diagonalized for each setting of the parameters $g_{\parallel}$, $g_{\perp}$, D_1, D_2, and J and χ_M evaluated at the temperatures where experimental data are available in a least-squares-fitting computer program.

Single-ion, zero-field splitting, $D\hat{S}_z^2$, for a Mn^{II} complex shows up as a splitting of the $^6A_1$ ground state of the Mn^{II} ion into three Kramers doublets ($M_S = \pm{}^1/_2, \pm{}^3/_2$, and $\pm{}^5/_2$). This splitting is dominated by a spin–orbit interaction between the $^6A_1$ state and quartet excited states such as $^4T_1$. Octahedral Mn^{II} complexes generally have D values less than ~0.1 cm^{-1}, for the $^4T_1$ excited state is at an appreciably higher energy than the $^6A_1$ ground state.[46] If the octahedral coordination geometry becomes tetragonally elongated or the Mn^{II} ion is in a square-pyramidal, five-coordinate site, D will become as large as ~1 cm^{-1} because the energy difference between the $^6A_1$ and $^4T_1$ states is reduced relative to the octahedral Mn^{II} case.[47-49]

The Mn^{III} ion in a tetragonally elongated coordination site with C_{4v} symmetry will have a $^5B_1$ ($b_2^1e^2a_1^1$) ground state with $^5A_1$ ($b_2^1e^2b_1^1$), ^5E ($b_2^1e^1a_1^1b_1^1$), and $^5B_2$ ($e^2a_1^1b_1^1$) excited states.[50] The ^5E and $^5B_2$ excited states can interact with the $^5B_1$ ground state to give a zero-field splitting of the $^5B_1$ state into the levels with $M_S = 0, \pm1$, and ±2. When $D < 0$, the $M_S = \pm2$ level is at the lowest energy, whereas when $D > 0$, then the $M_S = 0$ level is at the lowest energy. Depending on the magnitudes of distortion and crystal field interactions, triplet states can also be involved in a spin–orbit interaction with the $^5B_1$ ground state. D values for Schiff-base and porphyrin complexes of Mn^{III} have been found[51-53] to fall in the range of −1.0 to −3.0 cm^{-1}.

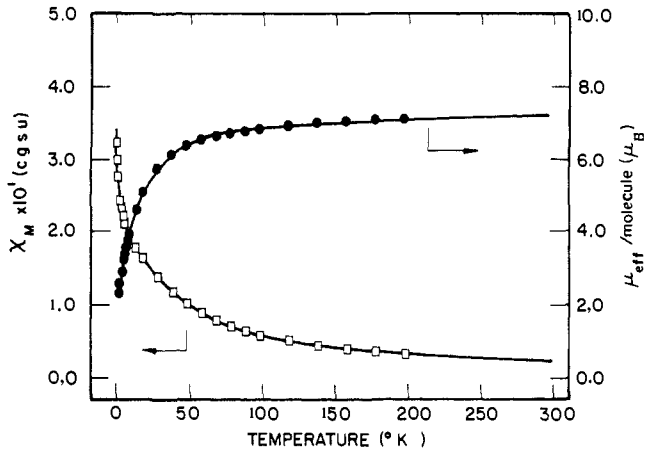

Figure 6. Plots of the molar paramagnetic susceptibility per molecule, χ_M, versus temperature and of the effective magnetic moment per molecule, μ_{eff}, versus temperature for $[LMn_2Br_3]\cdot{}^1/_2CH_2Cl_2$ (**3**). The solid lines illustrate the quality of the two best fits of the χ_M data to the full-matrix diagonalization approach including single-ion zero-field splitting. See the text for the fitting parameters.

Fits of the zero-field-splitting model to the temperature-dependent susceptibility data for $[LMn_2Cl_2Br]\cdot H_2O$ gave two fits of the quality illustrated by the lines in Figure 5. The fitting parameters were found to be $J = -1.80$ cm^{-1}, $D_1 = -1.37$ cm^{-1}, $D_2 = 1.93$ cm^{-1}, $g_{\parallel} = 1.92$, and $g_{\perp} = 1.84$ or $J = -1.88$ cm^{-1}, $D_1 = 10.4$ cm^{-1}, $D_2 = -1.53$ cm^{-1}, $g_{\parallel} = 1.91$, and $g_{\perp} = 1.80$, where D_2 and D_1 are for the Mn^{III} and Mn^{II} ions, respectively. It should be mentioned that if J is fixed to zero in this model, then fits to the data could only be found with magnitudes of the zero-field splitting exceeding 20 cm^{-1}. This is clearly unreasonable. For reasons discussed above the combination of $D_1 > 0$ and $D_2 < 0$ is favored. That is $D_1 = 10.4$ cm^{-1} for Mn^{II} and $D_2 = -1.53$ cm^{-1} for Mn^{III}. It should be mentioned that a range of fits of similar quality may be found for considerable variations in D_1, D_2. This feature of the fits will be discussed below.

Variable-temperature magnetic susceptibility data are given in the supplementary material and Figure 6 for mixed-valence $[LMn_2Br_3]\cdot{}^1/_2CH_2Cl_2$. Fitting χ_M for this compound to a theoretical equation which only accounts for an isotropic exchange interaction gives $J = -0.76$ cm^{-1} and $g = 1.97$ with TIP fixed at 200×10^{-6} cgsu per binuclear complex. Examination of Table S6 shows that this fit is not very good. As with the other $Mn^{II}Mn^{III}$ complex two different least-squares fits of the data for $[LMn_2Br_3]\cdot{}^1/_2CH_2Cl_2$ could be found to the matrix-diagonalization zero-field theoretical model. In one case the parameters $J = -1.1$ cm^{-1}, $D_1 = -1.2$ cm^{-1}, $D_2 = 4.6$ cm^{-1}, $g_{\perp} = 2.0$, and $g_{\parallel} = 2.0$ were obtained; in the other case $J = -1.1$ cm^{-1}, $D_1 = 4.81$ cm^{-1}, $D_2 = -2.26$ cm^{-1}, $g_{\parallel} = 2.10$, and $g_{\perp} = 1.98$. Both of the fits are as good as illustrated by the solid lines in Figure 6. The overall conclusion from these fittings is that J for complex **2** is ca. −1.8 to −2.0 cm^{-1} while that for complex **3** is −1.1 to −1.3 cm^{-1}, depending on the magnitudes of the single-ion zero-field splitting parameters D_1 and D_2.

(45) O'Connor, C. J. *Prog. Inorg. Chem.* **1982**, *29*, 203–283.
(46) Ballhausen, C. J. *Introduction to Ligand Field Theory*; McGraw-Hill: New York, 1962; pp 245–248.
(47) Yonetani, T. et al. *J. Biol. Chem.* **1970**, *245*, 2998.
(48) Dowsing, R. D.; Gibson, J. F.; Goodgame, M.; Hayward, P. J. *J. Chem. Soc. A* **1970**, 1133–1138.
(49) Birdy, R. B.; Goodgame, M. G. *J. Chem. Soc., Dalton Trans.* **1983**, 1469–1471.
(50) Dugad, L. B.; Behere, D. V.; Marathe, V. R.; Mitra, S. *Chem. Phys. Lett.* 1984, *104*, 353–356.
(51) (a) Kennedy, B. J.; Murray, K. S. *Inorg. Chem.* **1985**, *24*, 1552–1557. (b) Kennedy, B. J.; Murray, K. S. *Inorg. Chem.* **1985**, *24*, 1557–1560.
(52) Mathe, J.; Schinkel, C. J.; VanAnsted, W. A. *Chem. Phy. Lett.* **1975**, *33*, 528–531.
(53) (a) Behere, D. V.; Marathe, V. R.; Mitra, S. *Chem. Phys. Lett.* **1981**, *81*, 57–61. (b) Behere, D. V.; Mitra, S. *Inorg. Chem.* **1980**, *19*, 992–995. (c) Behere, D. V.; Mitra, S. *Inorg. Chem.* **1980**, *19*, 992–995.

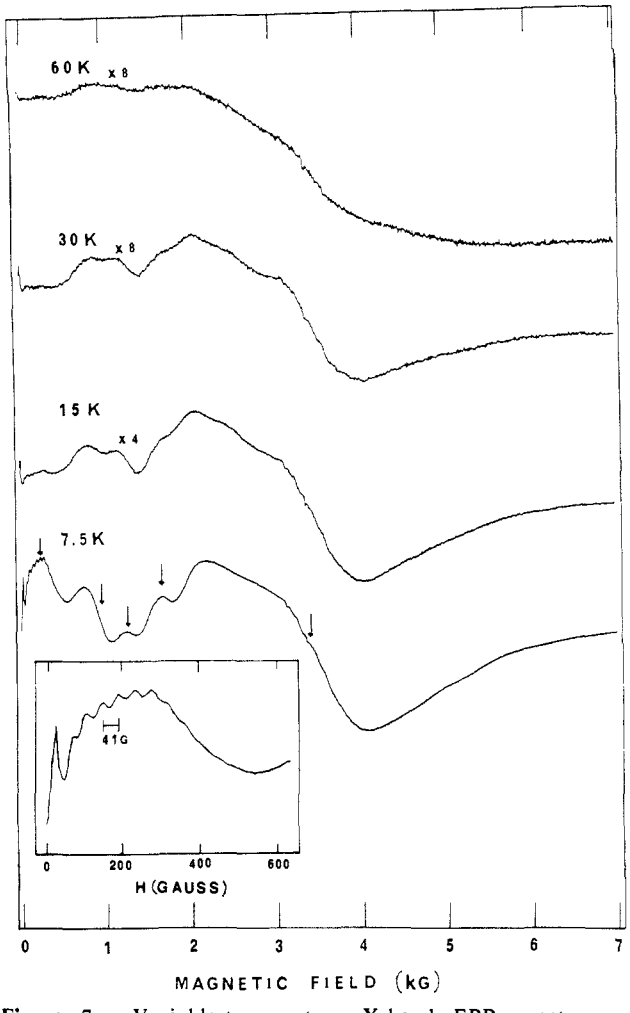

Figure 7. Variable-temperature X-band EPR spectrum of $[LMn_2Br_3]\cdot{}^1/_2CH_2Cl_2$ (**3**) in a 1:1 CH_2Cl_2/toluene glass. The 15, 30, and 60 K spectra were recorded at higher gains (indicated above the spectrum) relative to the gain employed at 7.5 K. The inset shows an expansion of the lowest field $g = 29$ signal obtained at 7.5 K.

Electron Paramagnetic Resonance Spectroscopy. X-band EPR spectra were run for polycrystalline and frozen glass samples of $[LMn_2Cl_2Br]\cdot H_2O$ and $[LMn_2Br_3]\cdot{}^1/_2CH_2Cl_2$. The two polycrystalline samples gave spectra with very broad signals, even when the samples were examined at ~3.2 K. In the case of both compounds a broad signal at $g \simeq 2$, as well as a considerably broader $g \simeq 4$ signal covering several thousand gauss were seen.

Two different glassing media were selected: a 1:1 dichloromethane/toluene (DT) mixture and a 1:1 methanol/toluene (MT) mixture. The temperature dependence of the X-band spectrum of $[LMn_2Br_3]\cdot{}^1/_2CH_2Cl_2$ in the DT glass is illustrated in Figure 7. It can be seen that at temperatures of 60 K or higher the spectral features are broad and poorly resolved. At temperatures below ~30 K some signals become better resolved. Finally, at 7.5 K several different signals can be discerned. A dominant feature in the spectrum is an asymmetric derivative-like signal centered at $g \simeq 2.0$ (arrows in Figure 7 correspond to the field positions). In addition to this signal, there are other transitions seen at the approximate field positions (arrows) which correspond to $g = 29.0$, 7.4, 5.4, and 4.1. As can be seen in the inset given in Figure 7 the low-field $g = 29.0$ signal exhibits 10 or more manganese hyperfine lines with a spacing of 41 G. It should be emphasized that the appearance of this hyperfine structure and, for that matter, all of the spectral features have been seen to be reproducible from one preparation to another of this DT glass. The X-band spectrum for the DT glass of $[LMn_2Cl_2Br]\cdot H_2O$ at 7.5 K looks similar to the spectrum in Figure 7; however, the low-field features and manganese hyperfine splittings are not nearly as well resolved.

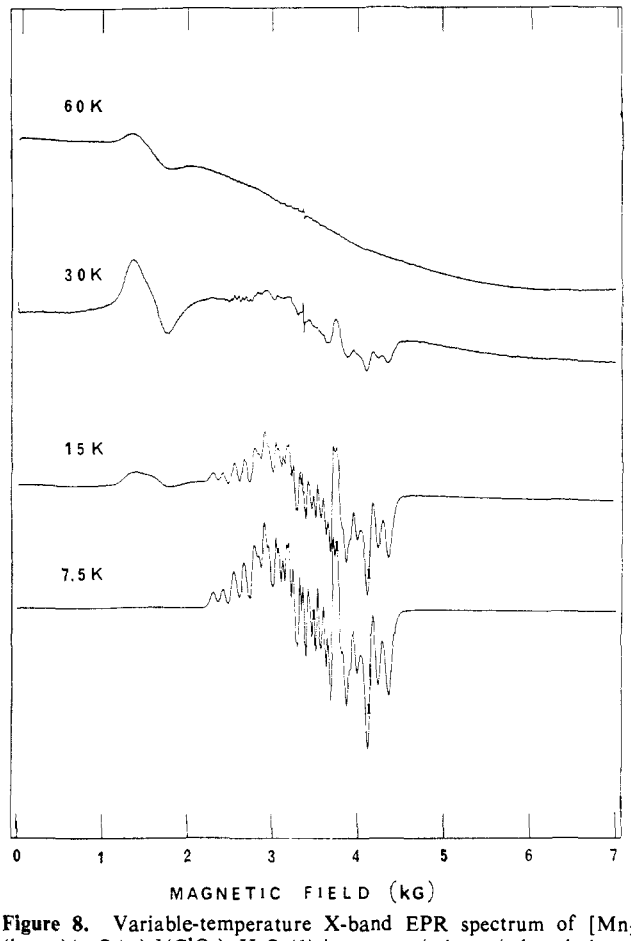

Figure 8. Variable-temperature X-band EPR spectrum of $[Mn_2(bpmp)(\mu\text{-}OAc)_2](ClO_4)_2\cdot H_2O$ (**1**) in acetone/toluene/ethanol glass.

An appreciation of the relative populations of complexes in the $S = {}^1/_2$ ground state and $S = {}^3/_2$, ${}^5/_2$, ${}^7/_2$, and ${}^9/_2$ excited states at 7.5 K and the temperature dependencies of these populations are needed to begin to understand the complicated spectrum shown in Figure 7. The Boltzmann populations of all the states at 4.2, 7.5, 15, 30, and 60 K for $[LMn_2Br_3]\cdot{}^1/_2CH_2Cl_2$ (**3**) and for a related structurally characterized[21] $Mn^{II}Mn^{III}$ complex $[Mn_2(bpmp)(OAc)_2](ClO_4)_2\cdot H_2O$ (**1**) were calculated by using $J = -1.3$ cm^{-1} or $J = -6.0$ cm^{-1}, respectively, values which were obtained by fitting the susceptibility data for these complexes. Even at 4.2 K, complex **3** has an appreciable amount (32.0%) of complexes in the $S = {}^3/_2$ excited state, compared to 62.8% in the $S = {}^1/_2$ ground state. For the temperature range studied, 7.5–60 K, the maximum population of the quartet state is near 7.5 K. Complex **1** has 99.6% population in the $S = {}^1/_2$ state at 4.2 K. When the temperature is increased to 15 K, complex **3** has appreciable population in all five of the states, whereas complex **1** has only 2.2% and 26.0% in the $S = {}^5/_2$ and ${}^3/_2$ excited states, respectively.

The temperature dependence[21,54] of the X-band spectrum of an acetone/toluene/ethanol (2:1:2) glass of complex **1**, as illustrated in Figure 8, is to be compared with that of complex **3** shown in Figure 7. Qualitatively the two temperature dependencies are similar. In both cases it is difficult to detect the $g \simeq 2.0$ signal when the temperature is increased to 60 K.

It is important to understand why the $g = 2$ signals in the glass EPR spectra for $Mn^{II}Mn^{III}$ complexes **2** and **3** do *not* show any resolved manganese hyperfine structure (see Figure 7), whereas the $g = 2$ signal for $Mn^{II}Mn^{III}$ complex **1** shows well-resolved hyperfine structure. The broadness of the $g = 2$ signals for complexes **2** and **3** could be attributable to several factors. First,

(54) Chang, H.-R.; Diril, H.; Nilges, M. J.; Zhang, X.; Potenza, J. A.; Schugar, H. J.; Hendrickson, D. N.; Isied, S. S. *J. Am. Chem. Soc.* **1988**, *110*, 625–627.

it is possible that these $g = 2$ signals are broad simply because these two complexes have appreciable populations in the $S = {}^3/_2$ and ${}^5/_2$ excited states, even at 7.5 K, and that complexes in these excited states have EPR signals where part of the signal falls in the $g = 2$ region. This does not seem to be the main cause of the broad $g = 2$ signals observed for 2 and 3. Close examination of the $g = 2$ region in the 15 K spectrum of **1** shows that there are *not* any new features present in the hyperfine structure which is still well resolved at 15 K. This is true even though there is 26.0% of the population of **1** in the $S = {}^3/_2$ excited state at 15 K. Thus, if there is any analogy between **3** and **1**, then it does *not* seem to be the 38.2% of $S = {}^3/_2$ excited state complexes for **3** at 7.5 K which lead to the very broad $g = 2$ signal for **3**.

A second possible origin of the broadness of the $g = 2$ signal for complex **3** is that there is some different overlapping of manganese hyperfine structure or more hyperfine lines than there is for **1**.

A third possible origin could arise from the proximity of the low-lying spin states to the ground doublet state. This could lead to contributions to the spin–lattice relaxation T_1 from Orbach relaxation processes[55] of the $|{}^1/_2,{}^1/_2\rangle$ to $|{}^1/_2,-{}^1/_2\rangle$ states via the higher spin states that are in the continuum of phonon energies. Such effects have been observed in the isoelectronic $Fe^{II}Fe^{III}$ sites found in 2Fe–2S proteins.[56,57] In this situation $1/T_1$ is proportional to $\Delta^3/[\exp(\Delta/kT) - 1]$, where Δ is the energy of the excited state relative to the relaxing ground state ($\simeq 160$ cm^{-1} for 2Fe–2S proteins). A detailed study of the temperature dependence of the line width of the EPR spectrum of 2Fe–2S centers leads to the conclusion that the main contribution to T_1 is via Orbach relaxation processes.[58] The observed EPR spectrum for such a $Fe^{II}Fe^{III}$ protein site is well resolved at low temperatures but broadens near 90 °C. A similar broadening and loss of resolution is seen in the spectrum of complex **1** but in a lower temperature range, 15–30 K. In complex **1** the excited spin states are closer to the $S = {}^1/_2$ ground state ($J = -6$ cm^{-1}) than in the 2Fe–2S proteins. If Orbach processes are responsible for the broadening with increasing temperature in this complex, then the temperature dependent factor $\exp(-\Delta/kT)$ will be modified leading to large variations in line width at a lower temperature range. The line width of **1** would be expected to increase by a factor of 20 between 7.5 and 30 K if the Orbach process was the only contributor to the spin–lattice relaxation. In the case of the EPR spectrum of complexes **2** and **3** where J is even smaller, −1.1 to −2.0 cm^{-1}, the observed EPR lines would be broad relative to those observed for **1** over the whole temperature studied and would only be of comparable width to those for **1** at 7.5 K at temperatures below 3 K. At 7.5 K the line widths of complex **2** would be ~ 5 times those of **1**.

A fourth possible origin of the broadness of the $g = 2$ signal for complexes **2** and **3** could be that complexes **2** and **3** in CH_2Cl_2/toluene glass are experiencing more **g** and/or **A** tensor strain than does complex **1** in the acetone/toluene/ethanol glass. If the $S = {}^1/_2$ ground state of a valence-trapped $Mn^{II}Mn^{III}$ complex has an isotropic **g** tensor, then $(2I_1 + 1)(2I_2 + 1) = (6)(6) = 36$ manganese hyperfine lines are expected. If the **g** tensor for the $S = {}^1/_2$ ground state is axial, then a total of 72 manganese hyperfine lines are expected; a rhombic **g** tensor should lead to 108 hyperfine lines. In an independent study[54] it has definitively been established that the $g = 2$ regions of the X- and Q-band EPR spectra of $Mn^{II}Mn^{III}$ complex **1** can be simulated by assuming that only the hyperfine structure for the z component of the **g** tensor was resolved in the X- and Q-band spectrum. That is, it was assumed that the hyperfine structure for the x and y components of the **g** tensor had broadened to the point of not contributing, except as a background, to the observed EPR spectra.

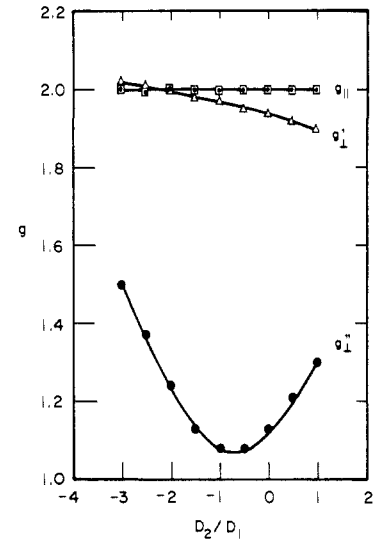

Figure 9. Plots of the dependencies $g_\parallel$ and $g_\perp$ for the $S = {}^1/_2$ ground state upon the ratio of single-ion zero-field splitting parameters for Mn^{III} (D_2) and Mn^{II} (D_1) ions in a binuclear $Mn^{II}Mn^{III}$ complex. The value of $g_\parallel$ depends neither on the ratio D_2/D_1 nor on the magnitude of the exchange parameter J. The value of $g_\perp$ does depend on J. The dependence of $g_\perp$ on D_2/D_1 is shown for $J = -6.0$ cm^{-1} ($g_\perp'$) and for $J = -1.0$ cm^{-1} ($g_\perp''$).

The differential broadening of transitions associated with the g_x, g_y components relative to the g_z component could be a reflection of **g** and **A** tensor strain effects and/or increased nitrogen superhyperfine interactions in the g_x and g_y directions. Such strain effects can result from a distribution of environments as found in a glass. In complexes **1**, **2**, and **3** an additional and important source of strain effects could arise from distributions in the magnitude of the isotropic exchange parameter J and single-ion zero-field splitting parameters D_1 and D_2. An inspection of the Hamiltonian energy matrix, formulated in the coupled basis set $|S_1,S_2,S,M_S\rangle$ as given in the supplementary material, shows that the components of the ground-state doublet $|S_1,S_2,{}^1/_2, \pm{}^1/_2\rangle$ are coupled to the $M_s = \pm{}^1/_2$ Kramers doublets of the $S = {}^3/_2$ and ${}^5/_2$ states by off-diagonal matrix elements of the form $\langle SM_S|\hat{H}_{ZFS}|S'M_S\rangle$ where $M_S = \pm{}^1/_2$, $S = {}^1/_2$, $S' = {}^3/_2$ or ${}^5/_2$, and $\hat{H}_{ZFS}$ is the zero-field splitting spin Hamiltonian. This leads to mixing of the $M_S = \pm{}^1/_2$ levels from the $S = {}^3/_2$ and ${}^5/_2$ states into the $S = {}^1/_2$ ground state. This mixing is dependent on the energy separation between the $S = {}^1/_2$, ${}^3/_2$, and ${}^5/_2$ states (determined by the isotropic exchange interaction) and the size of the matrix elements connecting them (determined by single-ion zero-field interaction terms). For the z direction this will lead to no variation of the g_z value with J, D_1, or D_2 because the g_z values are the same for the $M_S = \pm{}^1/_2$ Kramers doublets for all spin states (${}^1/_2$, ${}^3/_2$, ${}^5/_2$). On the other hand, for the g_x and g_y values of the $S = {}^1/_2$ ground state there is a marked dependence on J, D_1, and D_2. This is illustrated in Figure 9 for J values of −6.0 and −1.0 cm^{-1}. The variation of g_x and g_y with zero-field interactions decreases as the spin states diverge in energy so that the g_x and g_y values for complexes **2** and **3** are more sensitive to variations of J, D_1, and D_2 than they are for complex **1**.

In summary, the line broadening in the $g \simeq 2$ signals seen for glasses of **2** and **3** appears to arise from a combination of Orbach relaxation processes involving low-lying spin states and modulation of the g_x and g_y values by strain effects on the isotropic exchange and/or single-ion zero-field splitting.

A second feature of the frozen glass EPR spectra of complexes **2** and **3** is the additional lines observed at low temperature near $g = 29.0$, 7.4, 5.4, and 4.1. From a consideration of the populations of spin states in these systems it can be seen that the quartet $S = {}^3/_2$ state in **2** and **3** will be significantly occupied at 7.5 K. In the case of **3** it can be seen, Figure 7, that the signals at $g = 29.0$ in particular are maximized in intensity at 7.5 K as would be expected from the relative populations of the spin states. Ac-

(55) Orbach, R. *Proc. R. Soc. London, Ser. A* **1961**, *264*, 458–484.
(56) Palmer, G. In *Iron Sulfur Proteins*; Lovenborg, W., Ed.; Academic: New York, 1973; Vol. 2, pp 286–325.
(57) Gibson, J. F.; Hall, D. O.; Thornley, J. F.; Whatley, F. *Proc. Natl. Acad. Sci. U.S.A.* **1966**, *56*, 987–990.
(58) Gayda, J.-P.; Gibson, J. F.; Cammack, R.; Hall, D. O.; Mullinger, R. *Biochim. Biophys. Acta* **1976**, *434*, 154–163.

cordingly, these signals are attributed to the quartet state. Detailed studies of the EPR spectra of chromium(III) $S = {}^3/_2$ complexes by Toftlund and Pederson have delineated the criteria, in terms of g values, microwave frequency, and zero-field splitting, that lead to low-field signals from quartet states.[59] It is found that signals near $g \simeq 29$ will occur in X-band spectra ($h\nu \approx 0.3$ cm^{-1}) when splittings of the quartet state are in the range 0.4–0.6 cm^{-1}. For $[LMn_2Br_3]\cdot{}^1/_2CH_2Cl_2$ the energy difference between the $\pm{}^1/_2$ and $\pm{}^3/_2$ Kramers doublets of the $S = {}^3/_2$ state is calculated to be >5 cm^{-1} for the parameters selected from the fits to the magnetic susceptibility. Such an energy difference would lead to a relatively simple spectrum with signals near $g \simeq 4.0$ and 2.0. The zero-field splitting in the $S = {}^3/_2$ state is a complex function of the single-ion zero-field splittings D_1 and D_2 and the isotropic exchange coupling constant J. When $|J| \gg |D|$, then the splitting is dependent only on D_1 and D_2 as it is then possible to neglect the off-diagonal matrix elements connecting spin states. For molecules **2** and **3** this is not possible. A detailed examination was made of the range of D_1 and D_2 values ($D_1 > 0$, $D_2 < 0$) that would give rise to splittings in the quartet state of the order of 0.4 to 0.6 cm^{-1}. It was found that acceptable fits to the magnetic susceptibility of **3** were possible that would lead to such splittings. For example, the parameters $J = -1.1$ cm^{-1}, $D_1 = 1.5$ cm^{-1}, $D_2 = -1.77$ cm^{-1} lead to a splitting greater than 1 cm^{-1}, while $J = -1.1$ cm^{-1}, $D_1 = 1$ cm^{-1}, $D_2 = -3.0$ cm^{-1} gave a splitting of 1 cm^{-1}. Both of these fits are not significantly worse than the best fit found by least-squares fitting the susceptibility data. Values of D_1 and D_2 were found that would lead to a quartet splitting of 0.35 cm^{-1} ($J = -1.1$ cm^{-1}, $D_1 = 1.0$ cm^{-1}, $D_2 = -1.75$ cm^{-1}), and the fits to the magnetic susceptibility data were only slightly less good than those discussed above. The reason for this apparent nonunique fitting of the single-ion zero-field splitting parameters is due to the fact that the splitting of the quartet state really only depends on two parameters: J and some combination of D_1 and D_2. Using a combination of EPR spectra and knowledge of possible signs for D_1 and D_2 allows the range of possible values of the zero-field splitting to be estimated. A detailed study of the low-field EPR signals for $[LMnCl_2Br]\cdot H_2O$ also suggests that smaller values of D_1 and D_2 are required for compatibility with the EPR data.

An appreciably different frozen-glass X-band EPR spectrum is obtained for **3** in CH_3OH/toluene (see Figure 10) than is shown for **3** frozen in CH_2Cl_2/toluene (see Figure 7). The 77 K X-band spectrum of **3** in CH_3OH/toluene consists basically of a 6-line manganese hyperfine pattern, indicative of an interaction with one Mn^{II} ion, together with 10 weaker features found interspersed with the 6-line pattern. The 10 weaker features lying between the stronger $\Delta M_1 = 0$ allowed transitions are assignable to $\Delta M_1 = 1$ forbidden transitions.[60] This is verified by the appearance of the 77 K Q-band spectrum for a CH_3OH/toluene glass of complex **3**. In this Q-band spectrum the intensities of the ten $\Delta M_1 = 1$ forbidden lines are considerably less than those for the $\Delta M_1 = 0$ allowed transitions. When D (i.e., $D\hat{S}_z{}^2$) is of the same magnitude as the Mn^{II} ion hyperfine interaction parameter A (i.e., $D \sim A \simeq 0.01$ cm^{-1}), the $\Delta M_1 = 1$ forbidden transitions are seen and there are also unequal intensities in the six $\Delta M_1 = 0$ allowed lines (see X-band spectrum). The relative intensities of forbidden (I_f) to allowed (I_a) lines for the $\pm{}^1/_2$ Kramers doublet of a $S = {}^5/_2$ ion are given by the equation[61]

$$I_f/I_a = (512/15)(35/4 - m_1{}^2 + m_1)\left(\frac{D}{g\beta H}\right)^2 \qquad (2)$$

From this equation it can be understood why the relative intensities of the forbidden transitions decrease in going from X- to Q-band, for the value of ($g\beta H$) increases.

(59) Pederson, E.; Toftlund, H. *Inorg. Chem.* **1974**, *13*, 1603–1611.
(60) Weltner, W., Jr. *Magnetic Atoms and Molecules*; VanNostrand Reinhold Co., Inc.: New York, 1983; pp 266–277.
(61) Shaffer, J. S.; Farach, H. A.; Poole, C. P., Jr. *Phys. Rev.* **1976**, *B13*, 1869.

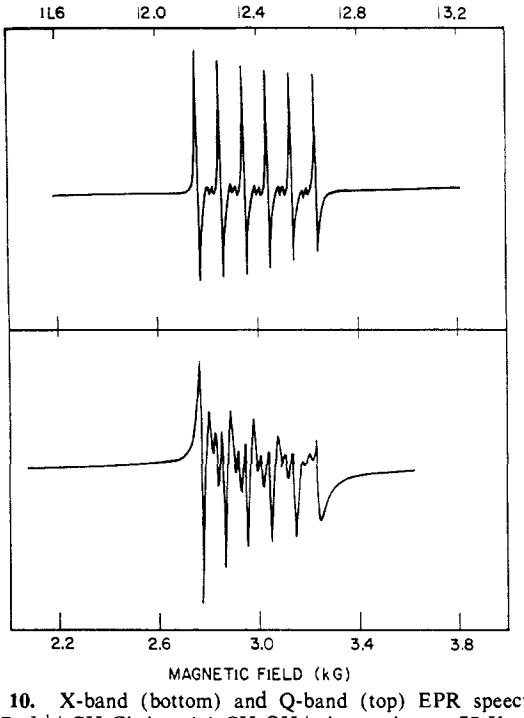

Figure 10. X-band (bottom) and Q-band (top) EPR speectra of $[LMn_2Br_3]\cdot{}^1/_2CH_2Cl_2$ in a 1:1 CH_3OH/toluene glass at 77 K.

The X- and Q-band spectra shown in Figure 10 are typical of Mn^{II} complexes.[60] Furthermore, double integration of the X-band spectrum shown in Figure 10, compared to a standard signal (1% $MnSO_4\cdot H_2O$ doped in anhydrous $MgSO_4$), showed that the intensity of this signal is of the appropriate intensity to account for the Mn^{II} ions in the amount of $[Mn^{II}Mn^{III}Br_3]\cdot{}^1/_2CH_2Cl_2$ dissolved. The signal is neither from an impurity nor from a $LMn^{II}{}_2Br_2$ complex. It is also relevant to note that this complex **3** can, in fact, be recrystallized from methanol. Decomposition of complex **3** does not occur in CH_3OH/toluene for at least 6 h; however, the EPR signal is quite changed over that found in the CH_2Cl_2/toluene glass. The only explanation for the appearance of the 77 K CH_3OH/toluene glass spectrum (Figure 10) is that CH_3OH has replaced the Br^-ion in $LMn^{II}(Br)Mn^{III}(Br)_2$ which bridges the Mn^{II} and Mn^{III} ions (see Figure 2). The replacement of this bridging Br^- ion by a nonbridging methanol ligand could severely attenuate the magnetic exchange interaction between the Mn^{II} and Mn^{III} ions. If they were effectively uncoupled, then the Mn^{II} ion may give the spectra shown in Figure 10. Monomeric Mn^{III} complexes do not readily give EPR signals.

Concluding Comments

There are two matters concerning binuclear mixed-valence manganese complexes which deserve comments relative to the electronic structure of the Mn_x site of the photosynthetic electron-transport chain. First, it is important to review how the magnitude and nature of magnetic exchange interactions change for the known binuclear $Mn^{II}Mn^{III}$ and $Mn^{III}Mn^{IV}$ complexes. Second, the EPR characteristics of the known binuclear $Mn^{II}Mn^{III}$ and $Mn^{III}Mn^{IV}$ complexes can be contrasted.

Five different binuclear $Mn^{II}Mn^{III}$ complexes and five different binuclear $Mn^{III}Mn^{IV}$ complexes are known. In Table VII are listed the magnetic exchange parameters and metric details of the bridges in these ten complexes. The first fact that becomes evident is that the antiferromagnetic exchange interactions for $Mn^{II}Mn^{III}$ complexes are quite weak relative to those for $Mn^{III}Mn^{IV}$ complexes. In the former case J ranges from −7.7 to +0.90 cm^{-1}. In the latter case J ranges from −40 to −220 cm^{-1}. Clearly there is a stronger antiferromagnetic interaction found for the $Mn^{III}Mn^{IV}$ complexes than for the $Mn^{II}Mn^{III}$ complexes. The $Mn^{II}Mn^{III}$ complexes have either two phenoxide oxygen atoms (together with one halide ion in the cases of complexes **2** and **3**) or one phenoxide oxygen atom with two acetates. Four of the $Mn^{III}Mn^{IV}$ complexes have two oxide bridges, a fifth possesses $(\mu\text{-O})_2(\mu\text{-OAc})$ bridging,

Table VII. Magnetic Exchange Parameters and Metric Details for Oxo- or Phenoxo-Bridging Groups of Binuclear $Mn^{II}Mn^{III}$ and $Mn^{III}M^{IV}$ Complexes[a]

compound	J, cm^{-1}	Mn–O–Mn angle(s); Mn–O bond distances of μ-O(Ph) bridge
$[(phen)_2Mn^{III}(\mu\text{-}O)_2Mn^{IV}(phen)_2](PF_6)_3\cdot CH_3CN$[b]	−148	84.0 (1)°; 1.808 (3) and 1.820 (3) Å
$[L'Mn^{III}Mn^{IV}(\mu\text{-}O)_2(\mu\text{-}OAc)](BPh_4)_2\cdot CH_3CN$[c]	−220	91.1 (1)°; 1.827 (5) and 1.808 (4) Å
$[(bipy)_2Mn^{III}(\mu\text{-}O)_2Mn^{IV}(bpy)_2](ClO_4)_3\cdot 3H_2O$[d]	−102 (−150 ± 7)[e]	1.784 and 1.854 Å
$[Mn^{III}Mn^{IV}(\mu\text{-}O)_2(Cl_2)(bpy)_2]\cdot 2CH_3CN$[f]	−114	94.52 (25)° and 94.35 (25)°; 1.827 (5), 1.843 (5), 1.805 (6), and 1.793 (5) Å
$[L''_2Mn^{III}Mn^{IV}(\mu\text{-}O)(\mu\text{-}OAc)_2](ClO_4)_3$[g]	−40	125.1 (3)°; 1.826 (6) and 1.824 (6) Å
$[Mn^{II}Mn^{III}(bpmp)(\mu\text{-}OAc)_2](ClO_4)_2\cdot H_2O$[h]	−6.0	114.4 (2)°; 2.193 (4) and 1.903 (4) Å
$[Mn^{II}Mn^{III}(bcmp)(\mu\text{-}OAc)_2](ClO_4)_2\cdot CH_2Cl_2$[i]	−7.7	112.1 (4)°; 2.17 (1) and 1.957 (9) Å
$[Mn^{II}Mn^{III}(bpy)_2(biphen)_2(biphenH)]\cdot 3CH_2Cl_2$[f]	+0.89	102.4 (4) and 97.1 (4)°; 2.124 (10), 2.112 (10), 1.956 (10), and 2.134 (10) Å
$[LMn_2Cl_2Br]\cdot H_2O$[j]	−1.7	93.6 (4)°; 1.941 (9), 1.931 (10), 2.386 (11), and 2.129 (10) Å
$[LMn_2Br_3]\cdot {}^1/_2CH_2Cl_2$[j]	−1.0	

[a] Abbreviations used are the following: phen is 1,10-phenanthroline; bpy is 2,2′-bipyridine; L′ is 1,4,7-triazacyclononane; L″ is *N,N′,N″*-trimethyl-1,4,7-triazocyclonone; bcmp⁻ is the same as bpmp⁻ (see drawing in text), except each of the bis(pyridylmethyl)amine moieties are replaced by a 1,4,7-triazacyclononane moiety; and biphenH_2 is 2,2′-biphenol. [b] Stebler, M.; Ludi, A.; Bürgi, H.-B. *Inorg. Chem.* **1986**, *25*, 4743–4750. [c] See ref 18. [d] See ref 17d. [e] See ref 17c. [f] Bashkin, J. S.; Schake, A. R.; Vincent, J. B.; Huffman, J. C.; Christou, G.; Chang, H.-R.; Li, Q.; Henrickson, D. N., submitted for publication. [g] Wieghardt, K.; Bossek, U.; Bonvoisin, J.; Beauvillain, P.; Girerd, J.-J.; Nuber, B.; Weiss, J.; Heinze, J. *Angew Chem., Int. Ed. Engl.* **1986**, *25*, 1030–1031. [h] See ref 21. [i] See ref 50. [j] This work.

and the sixth has $(\mu\text{-}O)(\mu\text{-}OAc)_2$ bridging. This sixth $Mn^{III}Mn^{IV}$ complex has a Mn–O–Mn angle of 125.1°, whereas the other Mn–O–Mn angles range from 91.1 to 96.0°. In the case of the structurally characterized $Mn^{II}Mn^{III}$ complexes the phenoxide bridging gives Mn–O–Mn angles in the range of 93.6–102.5°. Unless there is an appreciable difference in exchange propagating abilities between μ-oxide and μ-phenoxide moieties, there does not seem to be large enough differences in the bridge angles to explain why the antiferromagnetic exchange interactions in the $Mn^{III}Mn^{IV}$ complexes are so much stronger than those in the $Mn^{II}Mn^{III}$ complexes.

There seems to be two possible explanations for why the antiferromagnetic interactions observed for the $Mn^{III}Mn^{IV}$ complexes are greater than those observed for the $Mn^{II}Mn^{III}$ complexes. First, in converting a $Mn^{III}Mn^{IV}$ complex to a $Mn^{III}Mn^{II}$ complex two e_g*-type d-electrons are added to one metal center, and if everything else remained the same, the presence of these two additional d-electrons would likely increase the number of ferromagnetic exchange pathways relative to the manner of antiferromagnetic exchange pathways.[62] Thus, the interactions between the e_g*-type magnetic orbitals on the Mn^{II} ion and the t_{2g}-type magnetic orbitals on the Mn^{III} ion, as propagated by the $2p_x$, $2p_y$, and $2p_z$ oxygen orbitals, will largely be orthogonal and, consequently, ferromagnetic in origin.

The predominant exchange pathways for the $Mn^{II}Mn^{III}$ and $Mn^{III}Mn^{IV}$ complexes may also be modified by the symmetry of the individual metal ion sites. In the case of the Mn^{III} sites in complexes **1**, **2**, and **3** axial distortion (elongation) may be discerned that would lead to a stabilization of the d_{z^2} orbital relative to the $d_{x^2-y^2}$ orbital. This would lead to a singly occupied d_{z^2} orbital for the Mn^{III} sites. For Mn^{II} or Mn^{IV} the orbital occupancies $t_{2g}^3e_g^2$ and t_{2g}^3 are well defined, however, while the Mn^{III} sites the principal axis of quantization is not so clear. The z-axis of quantization for the Mn^{III} in complex **2**, for example, is expected to be approximately perpendicular to the Mn–Mn vector along the Mn–Cl1 direction. The magnetic orbitals of the Mn^{III} ion which would then be involved in superexchange pathways via the O atoms are the t_{2g} set, while for the Mn^{II} ion a complete range of t_{2g} and e_g magnetic orbitals would be available leading to both ferromagnetic and antiferromagnetic pathways. It should be noted that the relative axes of quantization for the two sites may not be parallel.

An examination of the data in Table VII indicates a second explanation for the stronger exchange interactions of $Mn^{III}Mn^{IV}$ complexes compared to $Mn^{II}Mn^{III}$ complexes. For those $Mn^{III}Mn^{IV}$ complexes which are *not* disordered in the solid state (see ref 2 in Table VII) the Mn^{III}–O bond lengths are only 0.04–0.07 Å longer than the Mn^{IV}–O bond lengths; the Mn^{III}–O bond lengths are in the range of 1.83–1.85 Å and the Mn^{IV}–O bond lengths are in the range of 1.78–1.80 Å. In contrast, the Mn^{II}–O bond lengths in the four structurally characterized $Mn^{II}Mn^{III}$ complexes are appreciably larger than either of the above Mn^{III}–O and Mn^{IV}–O bond lengths. The Mn^{II}–O bond lengths fall in the range of 2.17–2.39 Å. It is likely that this longer Mn^{II}–O bond length in a $Mn^{II}Mn^{III}$ complex would lead to a much weaker antiferromagnetic exchange interaction in $Mn^{II}Mn^{III}$ complexes compared to $Mn^{III}Mn^{IV}$ complexes.

It would not be unreasonable to expect pairwise $Mn^{II}Mn^{III}$ magnetic exchange interactions to be weaker antiferromagnetic interactions than pairwise $Mn^{III}Mn^{IV}$ interactions in the Mn_4 site of PSII. This could explain why the S_2 state of PSII gives rise to an EPR signal, whereas the S_0 state does not. The S_2 state is generally believed[7] to consist of a $Mn^{IV}Mn^{III}_3$ unit. If this is correct, the S_0 state is comprised of a $Mn^{II}Mn^{III}_3$ unit. Relatively strong antiferromagnetic interactions in the S_2 state could give a ground state (or a few low-lying states) which is fairly removed in energy from the large number of excited states. An EPR signal could then be observed at reasonable temperatures. This would be possible for the many excited states of the S_2 state would not be thermally populated and spin–lattice relaxation would not broaden the signal excessively. On the other hand, the relatively weak antiferromagnetic interactions between Mn^{II} and Mn^{III} ions in the S_0 state would lead to appreciable thermal populations not only in the ground state but also in many excited states even at liquid-helium temperature. Any EPR signals for the S_0 state would thus be broadened excessively due to Orbach relaxation processes and strain effects.

In keeping with the above suggestions about the EPR signals for the S_2 and S_0 states, it is important to note that the EPR signals for the $Mn^{II}Mn^{III}$ complexes in Table VII do broaden and become very hard to detect above ~60 K.[21,54] In contrast, the EPR signals for those binuclear $Mn^{III}Mn^{IV}$ complexes which have been studied as a function of temperature have been reported[18] to persist to temperatures as high as 298 K. More detailed variable-temperature EPR studies of these model complexes are needed.

Acknowledgment. D.N.H. is grateful for support from National Institutes of Health Grant HL13652 and C.G.P. is grateful for support from National Science Foundation Grant 85-03222. We have benefitted from conversations with Professors R. L. Belford and P. G. Debrunner.

Supplementary Material Available: Derivation of the matrix elements for the matrix diagonalization theoretical model for a $Mn^{II}Mn^{III}$ complex including single-ion zero-field interactions, complete listings of anisotropic thermal parameters and hydrogen-atom coordinates and isotropic thermal parameters for $[LMn_2Cl_2Br]\cdot H_2O$ (**2**) and LMn_2Cl_2 (**4**), experimental and theoretical-fit magnetic susceptibility data for compounds **2**, **3**, and **4**, and listings of coupled wave functions and non-zero matrix elements for matrix diagonalization model to fit susceptibility data for **2** and **3** (24 pages); listings of structure factors for **2** and **4** (38 pages). Ordering information is given on any current masthead page.

(62) Ginsberg, A. P. *Inorg. Chim. Acta* **1971**, *5*, 45–68.